Innovative Multi-Tagline Anti-swing And Positioning System: Dynamic Analysis and Experimental Validation for Slender-Beam Payloads in Offshore Environments

Maokai Sun[a,c], Shenghai Wang[a,*], Wanru Deng[b,c], Binteng Gu[c], Guangdong Han[a], Zhiming Yuan[c], Haiquan Chen[a], Yuqing Sun[a]

a Marine Engineering College, Dalian Maritime University, Dalian, China

b State Key Laboratory of Hydraulic Engineering Intelligent Construction and Operation, Tianjin University, Tianjin, China

c Department of Naval Architecture, Ocean and Marine Engineering, University of Strathclyde, Glasgow, UK

ABSTRACT

To address the challenges of low hoisting efficiency, high risk, and difficulty in achieving accurate positioning caused by the double-pendulum phenomenon of slender-beam payload (SBP) under rough sea conditions, a novel Multi-Tagline Anti-swing And Positioning System (MTAPS) is proposed in this study. A three-dimensional double-pendulum dynamic model of the MTAPS is established by using multi-body dynamics and Newton's classical mechanics. Furthermore, a decoupling control method is proposed to suppress the swing of the SBP. Numerous simulations and experiments have proved that the MTAPS can effectively reduce the swing of the SBP in an offshore environment. Under the set working conditions, the MTAPS can effectively reduce the swing of the SBP by more than 85%. The anti-swing device, based on the principles of this system, has been implemented in engineering practices, offering a novel approach for the rapid lifting and precise positioning of SBP in offshore settings.

Keywords: Marine crane; SBP; Double-pendulum; Multi-Tagline Anti-swing And Positioning System

1 Introduction

As the exploitation of marine resources advances, ships have become essential for transportation and various operational duties at sea. Among the critical deck equipment, marine cranes are increasingly utilized in diverse and novel operational contexts. These cranes are instrumental in activities such as the replenishment of ships (McTaggart et al., 2019), salvage operations for sunken vessels (Ham et al., 2018), installation offshore wind turbines (Zhao et al., 2019), and the handling of marine equipment (Zhang et al., 2017), as depicted in **Fig. 1**. Marine environmental forces, including wind, waves, and currents, induce nonlinear ship motions (Fossen, 1994), which interact with the inherently underactuated crane systems. As a result, payloads are prone to swinging during luffing and slewing maneuvers.

(a) Submersible recovery   (b) Carrier aircraft maintenance   (c) Marine equipment lifting

(d) Buoy lifting   (e) Wind turbine lifting   (f) Wind power installation
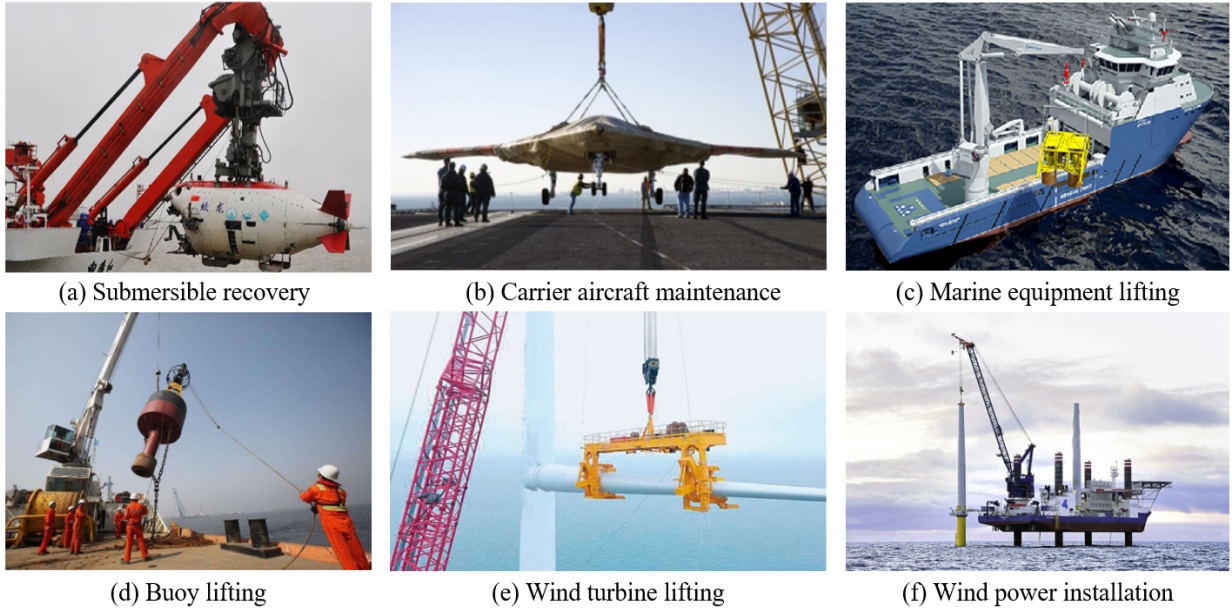
Fig. 1 Marine lifting operation

There has been comprehensive research on the control of swinging crane loads, as evidenced by extensive literature. Techniques explored include input shaping control Blackburn et al. (2010); (Singhose et al., 2008), sliding mode control (Hussein et al., 2020; Lee et al., 2006; Martin and Irani, 2021), and nonlinear control strategies (Ben Hazem et al., 2020; Cao and Li, 2024; Zhai et al., 2022). Concurrently, significant scholarly attention has been devoted to understanding crane dynamics, leading to the development of various modeling approaches. These approaches are generally categorized into three models: single-pendulum, double-pendulum, and constrained-pendulum.

In the single-pendulum approach, the hook and payload are assumed to be in close proximity, allowing them to be modeled as a single point mass. Dynamic models have been developed for various crane types, including overhead cranes (Aksjonov et al., 2015; Fatehi et al., 2014), gantry cranes (Renuka and Mathew, 2013; Singhose et al., 2002), rotary cranes (Sun et al., 2019b), offshore container cranes (Sun et al., 2019a), and offshore hydraulic cranes have been developed using the Lagrange method. Additionally, the dynamic model for boom knuckle crane has been established using screw theory (Cibicik, 2019).

When a crane transports an SBP, the system composed of the hook and the SBP often exhibits the typical characteristics of a double-pendulum system (Sun et al., 2024). The simplicity of the single-pendulum model fails to capture the intricate dynamics of such configurations. Consequently, various double-pendulum models have been derived for different crane types, including tower cranes (Vaughan et al., 2010), overhead cranes (Jaafar et al., 2019; Singhose et al., 2008; Sun et al., 2017), and boom cranes (Maleki and Singhose, 2012), which have been developed using the Lagrange method, as well as the double-pendulum dynamic model for bridge cranes has been formulated using the Kane method (Huang et al., 2015; Huang et al., 2014; Tang and Huang, 2016). Aside from the dynamic modeling of SBP,

(Ben Hazem et al., 2022; Hazem et al., 2023) utilized the SimMechanics toolbox/MATLAB to develop a dynamic model of a double link rotary pendulum system and introduced both a fuzzy linear quadratic regulator and a radial basis neuro-fuzzy linear quadratic regulator controller to effectively control the swing of this system. Experimental and simulation results have underscored the robustness and vibration suppression efficacy of these controllers.

During offshore crane lifting operations, cranes are frequently equipped with either passive or active mechanical systems to enhance operational efficiency and safety. (Kimiaghalam et al., 2000; Yuan et al., 1997) proposed a method known as Maryland Rigging, which utilizes the friction between pulleys and taglines to dissipate the energy of the swinging payload, thereby achieving swing suppression. (Parker et al., 2007) developed a kinematic model for the Rider Block Tagline System (a mechanical anti-swing device) and proposed a payload swing control method based on inverse kinematics. (Ku et al., 2013) employed a PD controller to control the tension of the ropes in real-time and built an experimental prototype to validate the effectiveness of the anti-swing mechanism. (Wang et al., 2021) proposed a Telescopic Sleeve Anti-swing Device for marine cranes and developed a dynamic model of this device. Hardware experiments demonstrated that this device achieved a swing reduction of over 70% for the payload. (Wang et al., 2023) proposed a rigid-flexible coupled cable-driven parallel mechanism to enhance the safety of offshore cargo transportation. The effectiveness of this mechanism was validated through experimental testing.

In recent years, the frequent installations of offshore wind power and the lifting of subsea pipelines have made the lifting of SBP increasingly common. However, such operations often encounter challenges including limited sway reduction, low operational efficiency, and high labor intensity. Currently, there is a notable gap in the dynamic modeling of SBP under ship-motion excitation with multi-tagline constraints. This study introduces a novel MTAPS that addresses the challenge of rapidly positioning long and heavy SBP during offshore lifting operations. Unlike previous research (Sun et al., 2024), the Anti-swing Positioning Device (ASPD) in this study is specifically designed with a quickly detachable fixture for SBP. The MTAPS features a straightforward mechanical structure and control algorithm, facilitating effective swing suppression of the double-pendulum system formed by the hook and SBP in any direction. This enables rapid transfer and precise positioning of SBP during offshore operations.

The contributions of this study are primarily in the following three areas:

(1) A novel MTAPS is proposed for lifting SBP under rough sea conditions, effectively enhancing the lifting efficiency and positioning accuracy of SBP. The kinetic model of the system, including the MTAPS and the ASPD, is developed using multi-body dynamics and Newtonian mechanics.

(2) Experimental data indicate that the average pendulum swing and projected area of the MTAPS can be reduced by more than 90% and 95%, respectively. When the MTAPS is employed, the reduction can exceed 85%.

(3) The MTAPS is highly versatile and can be retrofitted to existing marine cranes without impacting their functionality. Furthermore, the MTAPS significantly reduces the time required for the SBP to achieve relative stability, thereby facilitating the rapid transfer and precise positioning of SBP in offshore lifting operations.

The structure of this study is organized as follows: **Section 2** introduces the mechanical structure, working principle, and process of the MTAPS; **Section 3** details the kinematic and dynamic models of the ASPD and the MTAPS; **Section 4** analyzes the dynamic characteristics of the MTAPS lifting the SBP under sea states 4 and 5 through simulation; **Section 5** describes numerous hardware experiments, including the MTAPS lifting regular payloads and SBP; and **Section 6** concludes the findings.

2 The SBP lifting by the MTAPS

The SBP is a special type of payload where the center of mass is far away from the hook. Under rough sea conditions, the SBP and hook will show typical double-pendulum swing characteristics. The MTAPS proposed in this paper includes the MTAS and the ASPD, as shown in **Fig. 3**. The ASPD replaces the traditional hooks and will play a role in hoisting and clamping the SBP.

2.1 Previous research

Fig. 2-1 depicts the Double-Tagline Anti-swing System (DTAS) used previously on buoy ships for engineering operations, similar in structure to the Rider Block Tagline System. However, during the hoisting process, the anti-swing taglines on the same side tend to cause the hoisting tagline to tilt, resulting in increased wear on the crane's cable and diminished anti-swing effectiveness. **Fig. 2-2** introduces an enhanced Three-Tagline Anti-swing System (TTAS), which incorporates an additional anti-swing jib and tagline arranged in an inverted umbrella configuration. This design maintains the hoisting cable's vertical alignment, thereby reducing wear, yet struggles to maintain anti-swing efficiency as the crane's luffing angle increases. **Fig. 2-3** presents a solution involving a variable-angle electric cylinder to adjust the in-plane anti-swing jib in real time, and an additional anti-swing cable at the crane's base to improve sway control in all directions. The number of anti-swing taglines is adjustable based on operational conditions. Simulations have shown that with increasing mass and length of the SBP, the MTAS's effectiveness declines, necessitating a specialized lifting device designed specifically for the lifting and transportation of SBP in offshore environments.
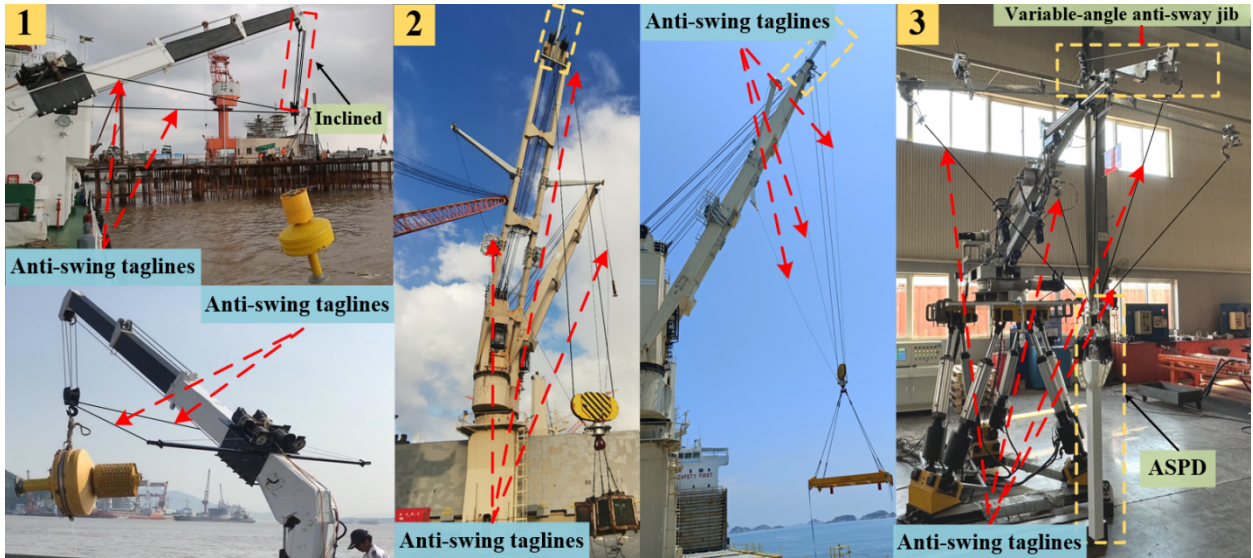
Fig. 2 Application of the DTAS on offshore cranes

2.2 The structure of the ASPD

The ASPD primarily consists of a stepping motor, a lead screw, a nut, and a multi-link gripping clip, all fabricated from lightweight materials to minimize the overall weight. The stepping motor manipulates the multi-link gripping clip by driving the lead screw, closing it when the SBP is hoisted into a suspension state. Concurrently, the MTAS activates, and in collaboration with the ASPD, works to mitigate the swing of the SBP in any direction.

2.3 The Structure and principle of the MTAS

The MTAS includes a mechanical structure, a power system, and a control system. As shown in **Fig. 3**, the Stewart platform (1) simulates the motion excitation of the ship, while the rotation mechanism (2) controls the crane's slewing motion. The winch (3) drives the MTAS, and electric cylinders (5 and 6) enable telescopic and luffing movements of the crane jib, respectively. Anti-sway jibs (7-9) are mounted on the crane jib, with the in-plane anti-sway jib (9) being adjustable in real-time by electric cylinder (10) to accommodate changes in the crane's luffing motion. This adjustment ensures that the in-plane component of the anti-swing cable I exerts sufficient force for optimal anti-swing performance. Anti-swing cables I, II, and III are connected to the three anti-sway jibs, while anti-swing tagline IV is positioned below the crane jib, forming a stable quadrilateral structure at the ASPD. The PLC control system gathers data from tension sensors (4), encoders, and swing angle measurement devices, processes this information, and sends control signals to the power system to maintain the tension within the anti-swing taglines within specified limits, effectively suppressing the SBP's swing in any spatial direction.
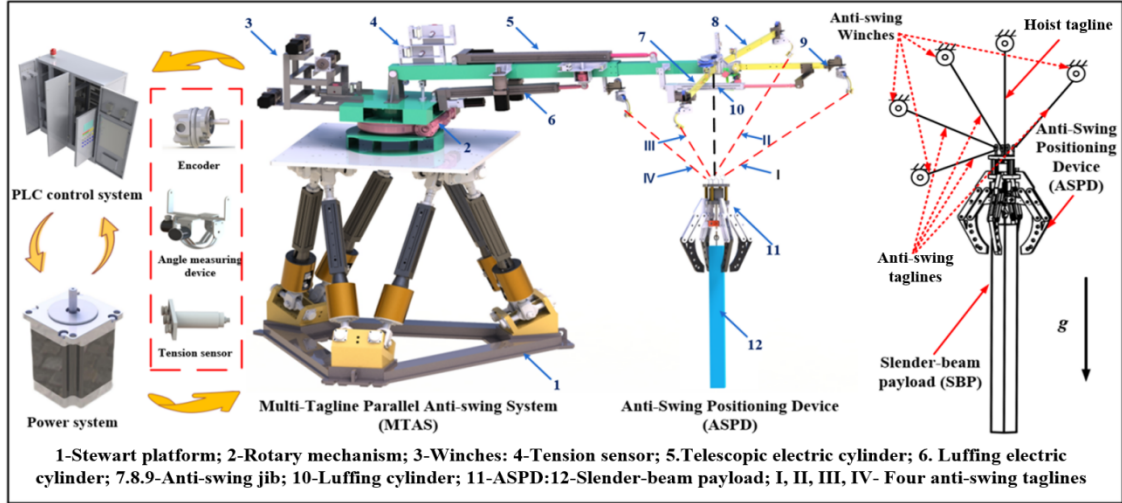
Fig. 3 Schematic diagram of the MTAPS

3 Dynamic modeling of the MTAPS

During the SBP lifting operations with the MTAPS, it is imperative that the four anti-swing taglines move synchronously. Failure to do so may result in the hoist tagline being pulled away, leading to excessive wear and diminished anti-swing performance. The anti-swing taglines must maintain sufficient tension to ensure a rapid response from the system. Throughout the lifting process, the ASPD and MTAS collaborate to optimize the anti-swing effectiveness. To facilitate this, dynamic modeling of the MTAPS is necessary, underpinned by the following assumptions.

(1) The jib and each anti-swing jib of the offshore crane are considered rigid.

(2) The SBP is modeled as a rigid body with an even mass distribution.

(3) The ASPD's multi-link grippers are rigid.

3.1 Kinematic analysis of the ASPD

As shown in **Fig. 4**, the ASPD includes a multi-link gripping clip, lead screws, stepper motors, sliders, and an anti-swing platform. The reciprocating motion of the multi-link gripping clip is achieved by the stepper motor driving the lead screw. The center of the lead screw features a through hole, allowing the main tagline to connect with the SBP. The anti-swing platform is equipped with bolt fasteners for connecting multiple anti-swing taglines. The ASPD replaces the traditional hook, thereby integrating the SBP with the MTAS. Link rod 2 is driven by the slider, which in turn drives link rods 1 and 2 to alternate between clamping and releasing the SBP. Mechanical analysis is conducted under static equilibrium conditions, with the sliding block considered as the force object. The driving force N of the screw nut, the supporting force F_d of link rod 3, and the pulling force F_{p1} of link rod 2 satisfy the static equilibrium conditions.
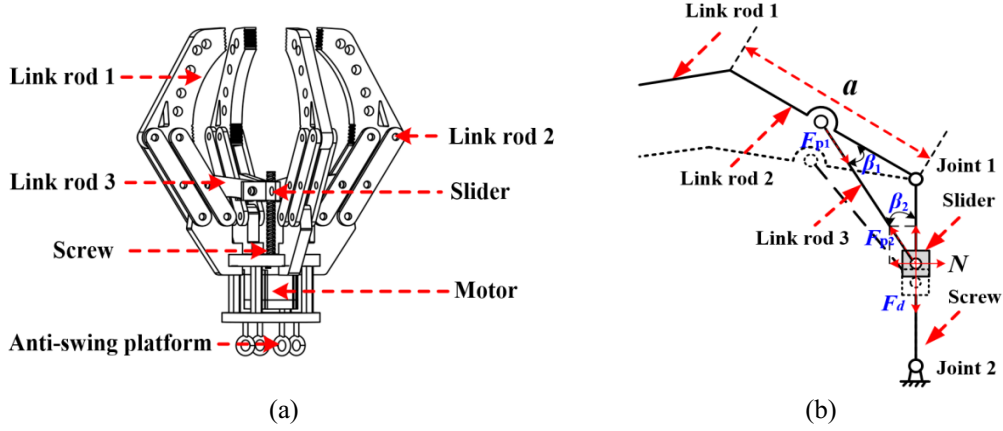
Fig. 4 3D and 2D structure diagrams of the ASPD

The static equilibrium equation can be written as:

$$F_{p_1} \cos \beta_2 = F_d \tag{1}$$

The torque equilibrium equation for Joint 1 is:

$$F_c a = \frac{1}{2} F_{p_2} \sin \beta_1 \tag{2}$$

In Eqs. (1) and (2), F_c is the force of the SBP on the connecting link rod 1, F_{p2} is the tension provided by the link rod 2, β_1 is the angle between the link rod 2 and 3, β_2 is the angle between the link rod 3 and screw, and a is the length of the link rod 2.

From **Fig. 4**, the link points of link rod 3 and link rod 2 are positioned at the center of link rod 2. The forces F_{p1} and F_{p2} are equal in magnitude and opposite in direction. Consequently, the following equations can be derived:

$$F_c = \frac{1}{2} Fd \frac{\sin \beta_1}{\cos \beta_2} \tag{3}$$

Fig. 5 is a mechanical analysis diagram of the lead screw and nut, where F_d is the driving force of the lead screw, F_m is the thrust transmitted by the motor torque, and N_m is the supporting force of the supporting parts. N_n is the thrust provided by the reaction force to the nut. The relationship between the motor torque and output F_c can be obtained by mechanical analysis of the anti-swing positioning device.
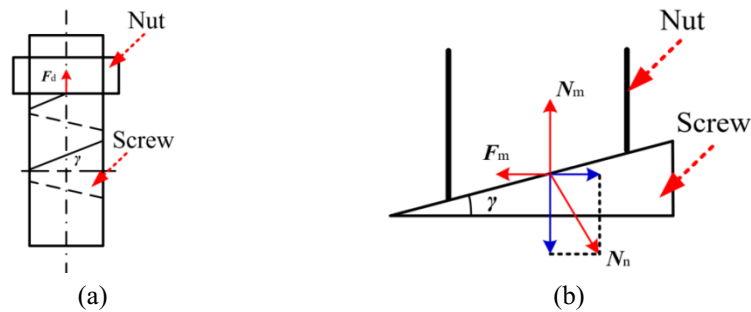
Fig. 5 Simplified drawing of lead screw and nut

Analyzing the forces in horizontal direction, we have

$$F_m = N_n \sin \gamma \tag{4}$$

where γ is the angle to the lead of the lead screw.

$$F_d = N_n \cos \gamma \tag{5}$$

$$F_d = \frac{F_m}{\tan \gamma} \tag{6}$$

$$F_m r = T_m \tag{7}$$

where r is the lead screw radius, T_m is the torque of the stepper motor, further arrangement of Eq. (6) and Eq. (7) can be obtained:

$$F_d = \frac{T_m}{r \tan \gamma} \tag{8}$$

Rearrange the formula can be obtained:

$$F_c = \frac{1}{2} T_m \frac{\sin \beta_1}{r \tan \gamma \cos \beta_2} \tag{9}$$

The small stepper motor in the ASPD provides only a small torque. The torque T_m of the ASPD is 0.22N·m, the lead screw radius r is 3 mm, and the lead angle γ is approximately 6°. When the multi-link gripping clip is in contact with the SBP, the angles β_1 and β_2 are 15° and 10°, respectively, resulting in a clamping force F_c of about 115 N. Therefore, the ASPD can provide sufficient clamping force for the SBP.

3.2 Kinematic model of the MTAS

In theoretical calculations and analyses, establishing the kinematic model of the MTAPS is crucial. This model serves as the foundation for position synchronization control and for determining the speed of the anti-swing taglines, which in turn helps select the appropriate winches. Subsequently, it is essential to develop both static and dynamic models of the system. These models are fundamental for examining the motion phenomena of the double-pendulum system and for analyzing the tension across multiple anti-swing taglines. Based on these dynamic analyses, a tension control scheme for the four anti-swing taglines is proposed. **Fig. 6** provides both 2D and 3D schematic diagrams of a offshore crane equipped with the MTAPS for lifting the SBP. As illustrated, $x_0y_0z_0$ is defined as the inertial reference frame, $x_1y_1z_1$ is the ship coordinates frame, and $x_2y_2z_2$ is the marine crane reference frame. The coordinates of the ASPD and the SBP in the space coordinate system are denoted as P_1 and P_2, respectively. O_2E represents the main jib of the marine crane, the length of the hoist tagline of P_1D is denoted L_1, and the distance between the center of mass of the hook and the center of mass of the SBP is denoted L_2. EF is the longitudinal anti-swing jib, HMN and HRS respectively represent the left and right lateral anti-swing jibs. P_1F, P_1N and P_1S are the anti-swing taglines corresponding to the three anti-swing jibs respectively, and P_1H is the anti-swing taglines arranged under the main

jib of the marine crane. $\theta_2 y$ represents the luff angle of the main jib, $\theta_2 z$ represents the slew angle of the crane, $\theta_1 x$, and $\theta_1 y$ correspond to the pitch and roll of the ship's motion, respectively. β_1 and β_2 are the longitudinal and lateral anti-swing jib angles, respectively. The in-plane angle and out-of-plane angle of the hoist tagline of the marine crane are represented by θ_1 and ψ_1, respectively. The in-plane angle and out-of-plane angle of the SBP are expressed by θ_2 and ψ_2, respectively. Moreover, $^0P_{P_1} = [x_P\ y_P\ z_P]^T$ represents the coordinates of P_1 in the $x_0 y_0 z_0$ coordinate system, and $L_{P_1 F}$ denotes the spatial distance between points F and P_1. L_1 is the length of the suspension tagline $P_1 D$, while L_2 is the distance between the center of mass of the SBP and the hook. Other tagline lengths in this paper are defined similarly.
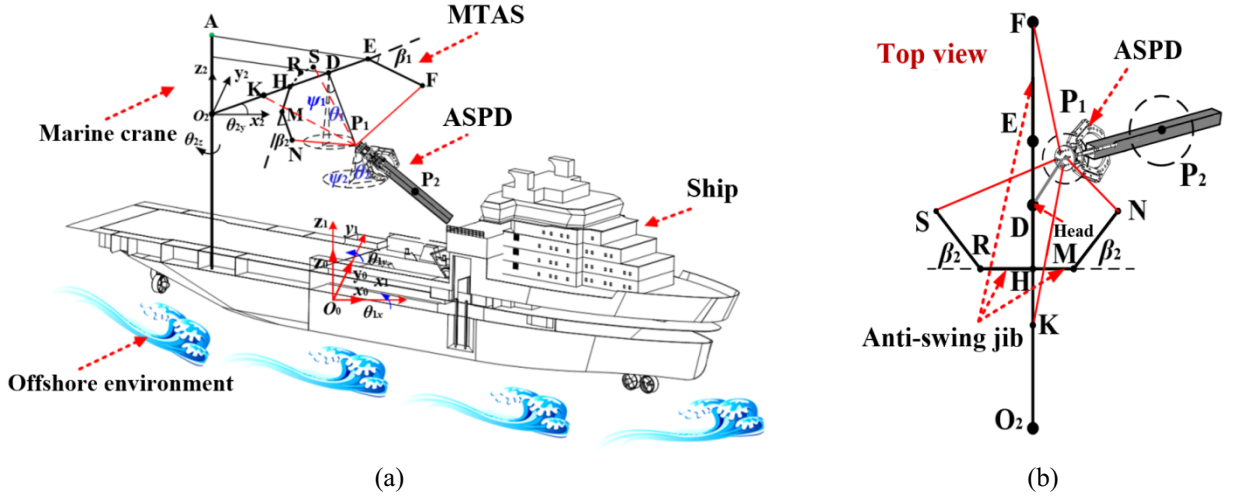
(a)   (b)
Fig. 6 Overview diagram of MTAPS lifting the SBP

Geometric analysis of **Fig. 6** yields the expressions for P_1 and P_2 in the coordinate system $x_2 y_2 z_2$.

$$^2P_{P_1} = {}^2P_{P_D} + \left[L_1 \sin\theta_1 \quad -L_1 \sin\psi_1 \quad -L_1 \cos\theta_1 \right]^T \tag{10}$$

$$^2P_{P_2} = {}^2P_{P_D} + \begin{bmatrix} L_1 \cos\psi_1 \sin\theta_1 + L_2 \cos\psi_2 \sin\theta_2 \\ -L_1 \sin\psi_1 - L_2 \sin\psi_2 \\ -L_1 \cos\psi_1 \cos\theta_1 - L_2 \cos\psi_2 \cos\theta_2 \end{bmatrix} \tag{11}$$

The coordinates of "D" in $x_2 y_2 z_2$ are given by the following expression:

$$P_D = \left[L_{O_2 D} \cos\theta_{2y} \quad 0 \quad L_{O_2 D} \sin\theta_{2y} \right]^T \tag{12}$$

The coordinates of points F, N, S and K can be clearly determined through geometric relations.

$$P_F = \left[L_{O_2 E} \cos\theta_{2y} + L_{EF} \cos\beta_1 \quad 0 \quad L_{O_2 E} \sin\theta_{2y} - L_{EF} \sin\beta_1 \right]^T \tag{13}$$

$$P_N = \left[L_{O_2 H} \cos\theta_{2y} + L_{MN} \sin\beta_2 \cos\theta_{2y} \quad -L_{HM} - L_{MN} \cos\beta_2 \quad L_{O_2 H} \sin\theta_{2y} - L_{MN} \sin\beta_2 \sin\theta_{2y} \right]^T \tag{14}$$

$$P_S = \left[L_{O_2 H} \cos\theta_{2y} + L_{MN} \sin\beta_2 \cos\theta_{2y} \quad L_{HM} + L_{MN} \cos\beta_2 \quad L_{O_2 H} \sin\theta_{2y} + L_{MN} \sin\beta_2 \sin\theta_{2y} \right]^T \tag{15}$$

$$P_K = \begin{bmatrix} L_{OK}\cos\theta_{2y} & 0 & L_{OK}\sin\theta_{2y} \end{bmatrix}^{\mathrm{T}} \tag{16}$$

When all the anti-swing taglines are under tension and in a taut state, the length expressions for anti-swing taglines L_{P_1F}, L_{P_1N}, L_{P_1S}, and L_{P_1K} can be obtained through geometric methods.

$$\begin{cases} L_{P_1F} = \sqrt{(x_F - x_{P_1})^2 + (y_F - y_{P_1})^2 + (z_F - z_{P_1})^2} \\ L_{P_1N} = \sqrt{(x_N - x_{P_1})^2 + (y_N - y_{P_1})^2 + (z_N - z_{P_1})^2} \\ L_{P_1S} = \sqrt{(x_S - x_{P_1})^2 + (y_S - y_{P_1})^2 + (z_S - z_{P_1})^2} \\ L_{P_1K} = \sqrt{(x_K - x_{P_1})^2 + (y_K - y_{P_1})^2 + (z_K - z_{P_1})^2} \end{cases} \tag{17}$$

R_x, R_y, and R_z are defined as rotation matrices with respect to the x, y, and z axes, respectively Baillieul (1987).

$$
{}^1_0R = \begin{bmatrix} 1 & 0 & 0 \\ 0 & \cos\theta_x & \sin\theta_x \\ 0 & -\sin\theta_x & \cos\theta_x \end{bmatrix} \quad
R_y = \begin{bmatrix} \cos\theta_y & 0 & -\sin\theta_y \\ 0 & 1 & 0 \\ \sin\theta_y & 0 & \cos\theta_y \end{bmatrix} \quad
R_z = \begin{bmatrix} \cos\theta_z & \sin\theta_z & 0 \\ -\sin\theta_z & \cos\theta_z & 0 \\ 0 & 0 & 1 \end{bmatrix} \tag{18}
$$

${}^m_nR$ is defined as the rotation matrix from the coordinate system $x_ny_nz_n$ to the coordinate system $x_my_mz_m$. Consequently, the rotation matrixes from $x_1y_1z_1$ and $x_2y_2z_2$ to $x_0y_0z_0$ can be obtained as follows:

$$
{}^1_0\mathbf{R} = \mathbf{R}_x(\theta_{1x})\mathbf{R}_y(\theta_{1y}) \tag{19}
$$

$$
{}^2_0\mathbf{R} = \mathbf{R}_x(\theta_{1x})\mathbf{R}_y(\theta_{1y})\mathbf{R}_z(\theta_{2z}) \tag{20}
$$

The coordinates D in the $x_0y_0z_0$ coordinate system can be ascertained using the subsequent mathematical equations:

$$
{}^0P_D = {}^0P_1 + {}^1_0R^{\mathrm{T}}\,{}^1P_2 + {}^2_0R^{\mathrm{T}}\,{}^2P_D \tag{21}
$$

The coordinates O_1 in $x_0y_0z_0$ are denoted by ${}^0P_1=[0\ 0\ 0]^{\mathrm{T}}$, and the coordinates O_2 in $x_2y_2z_2$ are represented by ${}^1P_2=[L_x\ L_y\ L_z]^{\mathrm{T}}$. The position of P_1 in the space coordinate system can be expressed as:

$$
\begin{aligned}
x_{P_1} &= L_x\cos\theta_{1y} + \cos\theta_{2z}\left(L_{P_1D}\cos\theta_1 + L_{O_2D}\cos\theta_{2y}\right)\cos\theta_{1y} + L_z\cos\theta_{1x}\sin\theta_{1y} + L_y\sin\theta_{1x}\sin\theta_{1y} + L_{PD}\sin\psi_o \\
&\quad \left(\cos\theta_{1x}\sin\theta_{2z} - \cos\theta_{2z}\sin\theta_{1x}\sin\theta_{1y}\right) + \left(L_{O_2D}\sin\theta_{2y} - L_{P_1D}\cos\theta_1\right)\left(\cos\theta_{1x}\cos\theta_{2z}\sin\theta_{1y} + \sin\theta_{1x}\sin\theta_{2z}\right)
\end{aligned} \tag{22}
$$

$$
\begin{aligned}
y_{P_1} &= \cos\theta_{1y}\left(L_{PD}\cos\psi_o\sin\psi_i + \cos\theta_{2y}L_{O_2D}\right)\sin\theta_{2z} - L_{PD}\sin\psi_o\left(\cos\theta_{1x}\cos\theta_{2z} + \sin\theta_{1x}\sin\theta_{1y}\sin\theta_{2z}\right) + \\
&\quad \left(L_{PD}\cos\psi_i\cos\psi_o - L_{O_2D}\sin\theta_{2y}\right)\left(\cos\theta_{2z}\sin\theta_{1x} - \cos\theta_{1x}\sin\theta_{1y}\sin\theta_{2z}\right) + L_y\cos\theta_{1x} - L_z\sin\theta_{1x}
\end{aligned} \tag{23}
$$

$$
\begin{aligned}
z_{P_1} &= \cos\theta_{1x}\cos\theta_{1y}\left(-L_{P_1D}\cos\theta_1 + L_z + L_{O_2D}\sin\theta_{2y}\right) - \left(L_x + L_{P_1D}\cos\theta_1 + L_{O_2D}\cos\theta_{2y}\right)\sin\theta_{1y} + \\
&\quad \left(L_y - L_{P_1D}\sin\theta_1\right)\cos\theta_{1y}\sin\theta_{1x}
\end{aligned} \tag{24}
$$

The ship's motion excitation is iteratively transferred to the crane's jib head using robotic methods. In the MTAPS, the excitation of the SBP double-pendulum system can be directly represented by the crane jib head. This reduces computational workload and simplifies representation in subsequent calculations.

3.2 Dynamic modeling of the MTPAS

Fig. 7 is a simplified schematic diagram of the system with the SBP. The ship-motion excitation is transmitted to the SBP through point D at the main jib head of the marine crane. Under this excitation, the ASPD and the SBP exhibit typical double-pendulum characteristics. The dynamic models of the MTAPS and crane system are established using the Newton-Euler method, which addresses the complexity of the Lagrange method in solving dynamic models. The tension of the main tagline is denoted by F_R, and the tensions of the anti-swing taglines I, II, III, and IV are denoted by F_1, F_2, F_3 and F_4, respectively. The masses of the ASPD and the SBP are represented by m_1 and m_2, respectively. The approximate centroid of the ASPD is denoted by P_1, and the centroid of the SBP is denoted by P_2.
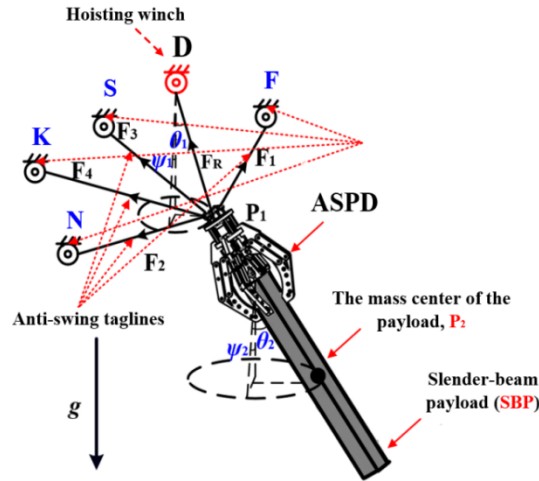
Fig. 7 Diagram illustrating the analysis of the double-pendulum system

Define $F_1=[F_{1x}\ F_{1y}\ F_{1z}]^T$, $F_2=[F_{2x}\ F_{2y}\ F_{2z}]^T$, $F_3=[F_{3x}\ F_{3y}\ F_{3z}]^T$, $F_4=[F_{4x}\ F_{4y}\ F_{4z}]^T$, $F_R=[0\ 0\ F_{Rz}]^T$, $G_P=[0\ 0\ mg]^T$. The tension components of anti-swing taglines are defined in the x_0, y_0, and z_0 directions.

$$\begin{cases} F_{1x} = |F_1| \cdot i_{1x} \\ F_{1y} = |F_1| \cdot i_{1y} \\ F_{1z} = |F_1| \cdot i_{1z} \end{cases} i_{1x} = \frac{(x_F - x_{P_1})}{L_{P_1F}}\ i_{1y} = \frac{(y_F - y_{P_1})}{L_{P_1F}}\ i_{1z} = \frac{(z_F - z_{P_1})}{L_{P_1F}} \tag{25}$$

$$\begin{cases} F_{2x} = |F_2| i_{2x} \\ F_{2y} = |F_2| i_{2y} \quad i_{2x} = \dfrac{(x_S - x_{P_1})}{L_{P_1 S}} \quad i_{2y} = \dfrac{(y_S - y_{P_1})}{L_{P_1 S}} \quad i_{2z} = \dfrac{(z_S - z_{P_1})}{L_{P_1 S}} \\ F_{2z} = |F_2| i_{2z} \end{cases} \tag{26}$$

$$\begin{cases} F_{3x} = |F_3| \cdot i_{3x} \\ F_{3y} = |F_3| \cdot i_{3y} \quad i_{3x} = \dfrac{(x_N - x_{P_1})}{L_{P_1 F}} \quad i_{3y} = \dfrac{(y_N - y_{P_1})}{L_{P_1 F}} \quad i_{3z} = \dfrac{(z_N - z_{P_1})}{L_{P_1 F}} \\ F_{3z} = |F_3| \cdot i_{3z} \end{cases} \tag{27}$$

$$\begin{cases} F_{4x} = |F_4| \cdot i_{4x} \\ F_{4y} = |F_4| \cdot i_{4y} \quad i_{4x} = \dfrac{(x_K - x_{P_1})}{L_{P_1 K}} \quad i_{4y} = \dfrac{(y_K - y_{P_1})}{L_{P_1 K}} \quad i_{4z} = \dfrac{(z_K - z_{P_1})}{L_{P_1 K}} \\ F_{4z} = |F_4| \cdot i_{4z} \end{cases} \tag{28}$$

The components representing the direction vector of the anti-swing tagline $P_1 F$ are i_{1x}, i_{1y} and i_{1z}. Similarly, the components representing the direction vector of the anti-swing tagline $P_1 N$ are i_{2x}, i_{2y} and i_{2z}. Furthermore, the direction vector of the anti-swing tagline $P_1 S$, which is symmetrical to $P_1 N$, is denoted by i_{3x}, i_{3y} and i_{3z}. The values for x_F, y_F, z_F, x_N, y_N, z_N, x_S, y_S and z_S can be obtained from **Eqs. (13)-(16)**.

From **Fig. 6**, it is evident that the two transverse anti-swing jibs and their corresponding taglines are completely symmetrical in space. Static stability in the y direction is achieved when the tension in both anti-swing taglines is equalized. Hence, it is sufficient to examine the static equilibrium solely along the x_0 and z_0 axes. At present, we are simulating the motion of the MTAPS, which is a system consisting of two pendulums that are restricted by anti-swing taglines made up of the ASPD and the SBP. The suspension tagline experiences tension along the x_0, y_0, and z_0 axes.

$$\begin{cases} F_{Rx} = |F_R| \cos \psi_1 \sin \theta_1 \\ F_{Ry} = |F_R| \sin \psi_1 \\ F_{Rz} = |F_R| \cos \psi_1 \cos \theta_1 \end{cases} \tag{29}$$

The forces exerted on the SBP in the x, y, and z directions are labelled as F_{Ex}, F_{Ey}, and F_{Ez}, correspondingly. The equation of motion for the ASPD can be expressed using Newton's second law.

$$\begin{cases} m_1 \ddot{x}_{p_1} = F_{1x} - F_{2x} - F_{3x} + F_{4x} - F_{Rx} + F_{Ex} \\ m_1 \ddot{y}_{P_1} = F_{1y} - F_{2y} - F_{3y} + F_{4y} + F_{Ry} - F_{Ey} \\ m_1 \ddot{z}_{p_1} = F_{1z} - F_{2z} - F_{3z} + F_{4z} + F_{Rz} - m_1 g - F_{Ez} \end{cases} \tag{30}$$

The acceleration at the ASPD can be determined by calculating the second derivative of the P_1 with respect to time.

$$\ddot{x}_{p_1} = \ddot{x}_D + L_1 \cos \theta_1 \left(\ddot{\theta}_1 \cos \psi_1 - 2 \dot{\theta}_1 \dot{\psi}_1 \sin \psi_1 \right) - L_1 \sin \theta_1 \left(\cos \psi_1 \left(\dot{\theta}_1^2 + \dot{\psi}_1^2 \right) + \ddot{\psi}_1 \sin \psi_1 \right) \tag{31}$$

$$\ddot{y}_{P_1} = \ddot{y}_D - \ddot{\psi}_1 L_1 \cos \psi_1 + \dot{\psi}_1^2 L_1 \sin \psi_1 \tag{32}$$

$$\ddot{z}_{P_1} = \ddot{z}_D + L_1\left(\cos\theta_1\cos\psi_1\left(\dot{\theta}_1^2 + \dot{\psi}_1^2\right) + \ddot{\psi}_1\cos\theta_1\sin\psi_1 + \ddot{\theta}_1\sin\theta_1\cos\psi_1 - 2\dot{\theta}_1\dot{\psi}_1\sin\theta_1\sin\psi_1\right) \tag{33}$$

Similarly, the acceleration at the center of mass of the SBP can be obtained by taking the second derivative of the coordinates of point P$_2$.

$$\ddot{x}_{P_2} = \ddot{x}_D + L_1\cos\theta_1(\cos\psi_1\ddot{\theta}_1 - 2\dot{\theta}_1\dot{\psi}_1\sin\psi_1) - L_1\sin\theta_1(\cos\psi_1(\dot{\theta}_1^2 + \dot{\psi}_1^2) + \ddot{\psi}_1\sin\psi_1) + L_2\cos\theta_2$$
$$(\cos\psi_2\ddot{\theta}_2 - 2\dot{\theta}_2\dot{\psi}_2\sin\psi_2) - L_2\sin\theta_2(\cos\psi_2(\dot{\theta}_2^2 + \dot{\psi}_2^2) + \ddot{\psi}_2\sin\psi_2) \tag{34}$$

$$\ddot{y}_{P_2} = \ddot{y}_D - L_1\cos\psi_1\ddot{\psi}_1 - L_2\cos\psi_2\ddot{\psi}_2 + L_1\dot{\psi}_1^2\sin\psi_1 + L_2\dot{\psi}_2^2\sin\psi_2 \tag{35}$$

$$\ddot{z}_{P_2} = \ddot{z}_D + L_2\cos\psi_2(\cos\theta_2(\dot{\theta}_2^2 + \dot{\psi}_2^2) + \ddot{\theta}_2\sin\theta_2) + L_1(\cos\theta_1\cos\psi_1\dot{\theta}_1^2 + \cos\theta_1\cos\psi_1\dot{\psi}_1^2) + \cos\psi_1$$
$$\sin\theta_1\ddot{\theta}_1 + \cos\theta_1\sin\psi_1\ddot{\psi}_1 - 2\dot{\theta}_1\dot{\psi}_1\sin\theta_1\sin\psi_1) + L_2(\cos\theta_2\ddot{\psi}_2 - 2\dot{\theta}_2\dot{\psi}_2\sin\theta_2)\sin\psi_2 \tag{36}$$

In order to simplify the formula, the tension of each anti-swing tagline in space is represented by the resultant force. The resultant force of the four anti-swing taglines can be established as follows:

$$f_x = F_{1x} - F_{2x} - F_{3x} + F_{4x} \tag{37}$$

$$f_y = F_{1y} - F_{2y} - F_{3y} + F_{4y} \tag{38}$$

$$f_z = F_{1z} - F_{2z} - F_{3z} + F_{4z} \tag{39}$$

The subsequent equation is deduced from Newton's second law:

$$\begin{cases} m_1\ddot{x}_{P_1} = f_x - |F_R|\cos\psi_1\sin\theta_1 + F_{Ex} \\ m_1\ddot{y}_{P_1} = f_y + |F_R|\sin\psi_1 - F_{Ey} \\ m_1\ddot{z}_{P_1} = f_z + |F_R|\cos\psi_1\cos\theta_1 - m_1g - F_{Ez} \end{cases} \tag{40}$$

F_{Ex}, F_{Ey} and F_{Ez} are the forces in x, y and z directions of the SBP respectively, which can be obtained by further analysis of the SBP.

$$\begin{cases} F_{Ex} = (m_2g\cos\theta_2\cos\psi_2 + \dfrac{1}{2}m_2\left(\dfrac{\dot{\psi}_2\sin\psi_2\cos\theta_2 + \dot{\theta}_2\sin\theta_2\cos\psi_2}{\sqrt{1-\cos\psi_2\cos\theta_2}}\right)^2 L_2)\cos\psi_2\sin\theta_2 \\[4mm] F_{Ey} = (m_2g\cos\theta_2\cos\psi_2 + \dfrac{1}{2}m_2\left(\dfrac{\dot{\psi}_2\sin\psi_2\cos\theta_2 + \dot{\theta}_2\sin\theta_2\cos\psi_2}{\sqrt{1-\cos\psi_2\cos\theta_2}}\right)^2 L_2)\sin\psi_2 \\[4mm] F_{Ez} = (m_2g\cos\theta_2\cos\psi_2 + \dfrac{1}{2}m_2\left(\dfrac{\dot{\psi}_2\sin\psi_2\cos\theta_2 + \dot{\theta}_2\sin\theta_2\cos\psi_2}{\sqrt{1-\cos\psi_2\cos\theta_2}}\right)^2 L_2)\cos\psi_2\cos\theta_2 \end{cases} \tag{41}$$

Substituting Eqs. (37)-(39) and (41) into Eq. (40), and then eliminating the variable F_R from the system of Eq. (40), we have:

$$\begin{cases} (f_x + F_{Ex} - m_1\ddot{x}_{P_1})\tan\psi_1 = (m_1\ddot{y}_{P_1} - f_y + F_{Ey})\sin\theta_1 \\ (m_1\ddot{y}_{P_1} - f_y + F_{Ey})\cos\theta_1 = (m_1\ddot{z}_{P_1} - f_z + m_1g)\tan\psi_1 \end{cases} \tag{42}$$

The accelerations θ_1 and ψ_1 at ASPD can be expressed as:

13

$$\ddot{\theta}_1 = -\sec\psi_1((F_{Ex}+f_x)\cos\theta_1+(-F_{Ex}+f_z)\sin\theta_1-m_1(\cos\theta_1\ddot{x}_D+(g+\ddot{z}_D)\sin\theta_1-2L_1\dot{\theta}_1\dot{\psi}_1\sin\psi_1))/m_1L_1 \tag{43}$$

$$\ddot{\psi}_1 = -\cos\theta_1(F_{Ez}-f_z+m_1g+m_1\ddot{z}_D)\sin\psi_1-\sin\theta_1\sin\psi_1(F_{Ex}+f_x-m_1\ddot{x}_D)+\cos\psi_1$$
$$(F_{Ez}-f_y+m_1\ddot{y}_D-L_1m_1\theta_1^2\sin\psi_1)/m_1L_1 \tag{44}$$

To solve for the swing angle of the SBP, it is necessary to perform an independent force analysis on the SBP. By analyzing the moment of the SBP, we can determine its angular acceleration.

$$I_{P_2}\ddot{\theta}_2=\sum\tau=(R_{2x}-F_{gx})\cos\psi_2\cos\theta_2L_2+R_{2z}\cos\psi_2\sin\theta_2L_2 \tag{45}$$

$$I_{P_2}\ddot{\psi}_2=\sum\tau=-(R_{2y}-F_{gy})\cos\theta_2\cos\psi_2L_2+R_{2z}\sin\psi_2L_2 \tag{46}$$

In the formula, F_{gx} and F_{gy} respectively represent the force exerted by the ASPD on the SBP. The torque of the SBP can be calculated using Newton's second law.

$$\begin{cases} m_2\ddot{x}_{P_2}=\sum Fx=R_{2x} \\ m_2\ddot{y}_{P_2}=\sum Fy=R_{2y} \\ m_2\ddot{z}_{P_2}=\sum Fy=R_{2z}-m_2g \end{cases} \tag{47}$$

The axis of rotation for the SBP is located at the hook, therefore, the moment of inertia of the SBP can be expressed as:

$$I_{P_2}=\frac{1}{12}ML^2=\frac{1}{12}m_2(2L_2)^2=\frac{1}{3}m_2L_2^2 \tag{48}$$

By substituting Eqs. (34)-(36), (41), and (47) into Eq. (45) and (46), After performing the calculations, one can obtain the angular accelerations angle θ_2 and ψ_2 at the center of mass of the SBP.

$$\ddot{\theta}_2=(-3\cos\psi_2(m_2\ddot{x}_D+m_2L_1\cos\theta_1(\cos\psi_1\ddot{\theta}_1-2\dot{\theta}_1\dot{\psi}_1\sin\psi_1)-m_2L_1\sin\theta_1(\cos\psi_1(\dot{\theta}_1^2+\dot{\psi}_1^2)+\ddot{\psi}_1\sin\psi_1)$$
$$+m_2L_2\cos\theta_2(\cos\psi_2\ddot{\theta}_2-2\dot{\theta}_2\dot{\psi}_2\sin\psi_2)-m_2L_2\sin\theta_2(\cos\psi_2(\dot{\theta}_2^2+\dot{\psi}_2^2)+m_2\ddot{\psi}_2\sin\psi_2-f_G)\cos\theta_2+(m_2\ddot{z}_D$$
$$-m_2L_2\cos\psi_2(\cos\theta_2(\dot{\theta}_2^2+\dot{\psi}_2^2)+\ddot{\theta}_2\sin\theta_2)+L_1(\cos\theta_1\cos\psi_1\dot{\theta}_1^2+\cos\theta_1\cos\psi_1\dot{\psi}_1^2)+\cos\psi_1\sin\theta_1\ddot{\theta}_1+\cos\theta_1$$
$$\sin\psi_1\ddot{\psi}_1-2\dot{\theta}_1\dot{\psi}_1\sin\theta_1\sin\psi_1)+L_2(\cos\theta_2\ddot{\psi}_2-2\dot{\theta}_2\dot{\psi}_2\sin\theta_2)\sin\psi_2)\sin\theta_2+m_2g\sin\theta_2))/m_2L_2 \tag{49}$$

$$\ddot{\psi}_2=-3((m_2\ddot{y}_D-m_2L_1\cos\psi_1\ddot{\psi}_1-m_2L_2\cos\psi_2\ddot{\psi}_2+m_2L_1\dot{\psi}_1^2\sin\psi_1+m_2L_2\dot{\psi}_2^2\sin\psi_2-f_{ZG})\cos\theta_2\cos\psi_2+m_2\ddot{z}_D$$
$$+m_2L_2\cos\psi_2(\cos\theta_2(\dot{\theta}_2^2+\dot{\psi}_2^2)+m_2\ddot{\theta}_2\sin\theta_2)+m_2L_1(\cos\theta_1\cos\psi_1\dot{\theta}_1^2+\cos\theta_1\cos\psi_1\dot{\psi}_1^2)+m_2\cos\psi_1\sin\theta_1\ddot{\theta}_1$$
$$+m_2\cos\theta_1\sin\psi_1\ddot{\psi}_1-2m_2\dot{\theta}_1\dot{\psi}_1\sin\theta_1\sin\psi_1)+m_2L_2(\cos\theta_2\ddot{\psi}_2-2\dot{\theta}_2\dot{\psi}_2\sin\theta_2)\sin\psi_2\sin\psi_2+m_2g\sin\psi_2)/m_2L_2 \tag{50}$$

4 Analysis of the dynamic characteristics of the MTPAS

Similar to the damping principle, the MTAPS uses four anti-swing taglines to dissipate energy and achieve precise positioning of the SBP. Each anti-swing tagline is driven by a corresponding winch, with tension sensors and encoders integrated into the MTAPS. The control system can control the anti-swing taglines in real-time by collecting, processing, and outputting signals. It processes the tension and encoder signals and sends commands to the winches for real-time control of the anti-

swing taglines. anti-swing taglines I and IV restrain the in-plane angle of the SBP, while anti-swing taglines II and III control the out-of-plane angle. A pre-tension is set for each anti-swing tagline within a control system, ensuring that the flexible anti-swing taglines remain taut in any states. This ensures a quick response to changes in tagline tension and prevents taglines from slipping off the reel.

$$\begin{cases} if \quad \dot{\psi}_1 > 0 \quad F_{3y} = \delta_{3y} \quad F_{2y} = -K\psi_1 - B\dot{\psi}_1 + F_{3y} \\ if \quad \dot{\psi}_1 \leq 0 \quad F_{2y} = \delta_{2y} \quad F_{3y} = F_{2y} + K\psi_1 + B\dot{\psi}_1 \\ if \quad \dot{\theta}_1 > 0 \quad F_{1x} = \delta_{1x} \quad F_{4x} = -K\theta_1 - B\dot{\theta}_1 + F_{1x} \\ if \quad \dot{\theta}_1 \leq 0 \quad F_{4x} = \delta_{4x} \quad F_{1x} = F_{4x} + K\theta_1 + B\dot{\theta}_1 \end{cases} \tag{51}$$

F_{2y} and F_{3y} represent the components of F_2 and F_3 along the y-axis, while F_{1x} and F_{4x} represent the components of F_1 and F_4 along the x-axis. Here, $K>0$, $B>0$ are the stiffness and damping coefficients of the MTAPS, respectively. δ_{2y} and δ_{3y} are the components of the pre-tightening force of anti-swing taglines II and III in the y-axis direction, respectively, and δ_{1x} and δ_{4x} are the components of the pre-tightening force of anti-swing taglines I and IV in the x-axis direction, respectively. In terms of out-of-plane angle swing suppression, when the SBP swings to point N, anti-swing tagline II dissipates the energy of the SBP, while anti-swing tagline III on the opposite side only maintains a certain pre-tightening force to prevent loosening. Anti-swing taglines I and IV are responsible for energy dissipation in the in-plane direction of the SBP.

The four anti-swing taglines must always maintain a certain tension; otherwise, the phenomenon of tagline loosening will occur. The tension-setting method for multiple anti-swing taglines is as follows:

$$\begin{cases} F_{1s} - \delta_1 \leqslant |\boldsymbol{F_1}| \leqslant F_{1s} + \delta_1 \\ F_{2s} - \delta_2 \leqslant |\boldsymbol{F_2}| \leqslant F_{2s} + \delta_2 \\ F_{3s} - \delta_3 \leqslant |\boldsymbol{F_3}| \leqslant F_{3s} + \delta_3 \\ F_{4s} - \delta_4 \leqslant |\boldsymbol{F_4}| \leqslant F_{4s} + \delta_4 \end{cases} \tag{52}$$

The programming and simulation software of this study is Matlab/Simulink, and the solver used in Matlab/Simulink is Ode 45. The pre-tension of the four anti-swing taglines I, II, III and IV are respectively expressed as F_{1s}, F_{2s}, F_{3s} and F_{4s}. The tension thresholds of the four anti-swing taglines are δ_1, δ_2, δ_3 and δ_4, respectively. It is worth noting that multiple anti-swing taglines directly control the anti-swing of the ASPD, and the ASPD transfers binding forces of the anti-swing system to the SBP through a multi-link gripping clip.

Section 4 presents the results of the simulation analysis performed under conditions of sea state 4 and sea state 5. The parameters for sea state 4 include a roll amplitude of 6° with a period of 13 seconds, and a pitch amplitude of 1.5° with a period of 6 seconds. For sea state 5, the parameters are a roll amplitude of 9° with a period of 14 seconds, and a pitch amplitude of 2.5° with a period of 6 seconds. These parameters are based on ships with a length of 560 feet (Love, 2003). The

crane parameters in **Tab. 1** are derived from a marine crane of COSCO Shipping, and the installation positions of each anti-swing jib are determined according to engineering experience.

Table. 1 The default system parameters

Parameters	value	Parameters	value
L_{EF}/m	6.4	β_1/°	0
L_{HM}/m	2.5	β_2/°	30
L_{MN}/m	2.5	g/m/s²	9.8
L_{O_2H}/m	18	L_x/m	0
L_{O_2D}/m	29	L_y/m	0
L_{O_2E}/m	30	L_z/m	1.5
L_{O_2K}/m	15	θ_{2y}/°	60

4.1 Dynamic simulation of the MTAPS lifting the SBP

Figs. 8 and **9** present the dynamic response curves for sea states 4 and 5, respectively, while **Fig. 10** contrasts the projection areas with and without the anti-swing system. **Tab. 2** summarizes the simulation data, demonstrating that both the MTAS and the MTAPS significantly reduce the swing of the SBP. Under sea state 4, the MTAS and MTAPS achieve average swing angle reduction ratios of 74% and 83%, respectively. Similarly, the projected area reduction ratios for the MTAS and MTAPS are 71% and 82%, respectively. The MTAPS exhibits more than a 10% improvement over the MTAS in both swing angle and projected area reduction, enabling the SBP to stabilize more rapidly. The four anti-swing taglines of the MTAS converge at the hook, where the swing energy of the SBP is dissipated through its interaction with the conventional hook, effectively suppressing the swing. In contrast, the MTAPS employs an anti-swing positioning device instead of a hook, and the four anti-swing taglines connect to this device. The binding force from the multiple anti-swing taglines is transmitted to the SBP through a multi-link gripping clip, thereby enhancing the anti-swing effect on the SBP, particularly for payloads that are longer and heavier.

(a)   (b)

(c)
          (d)
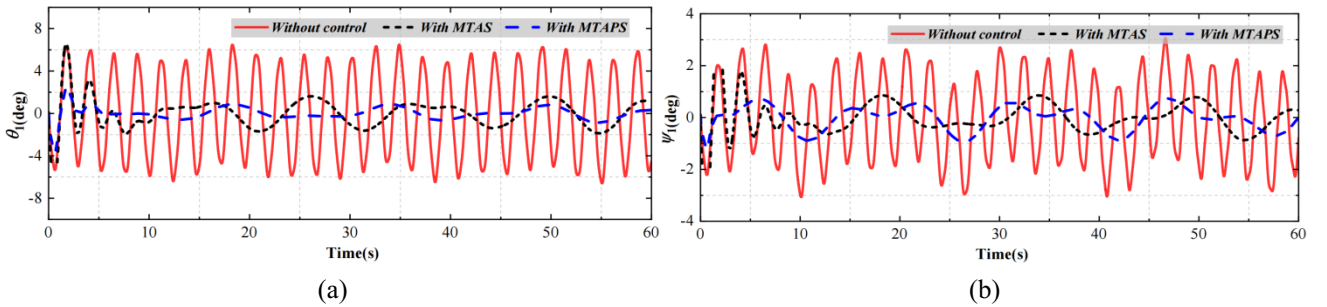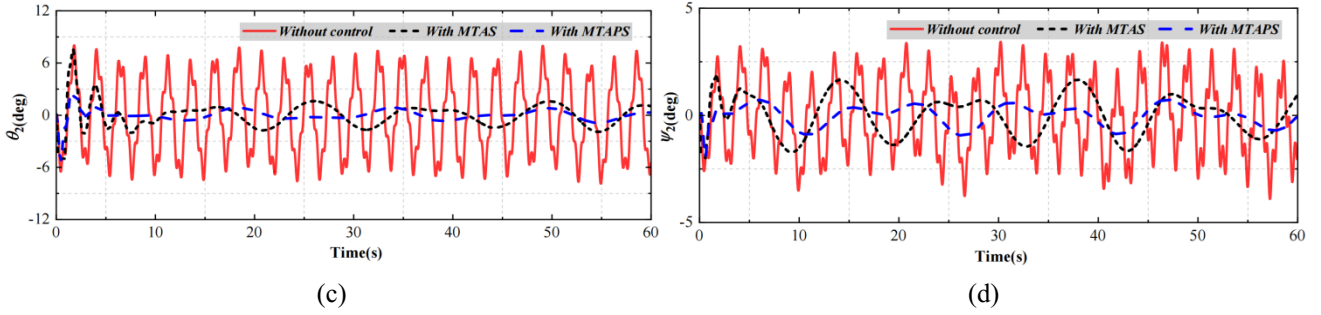
Fig. 8 Contrastive analysis with and without anti-swing under sea state 4. (a) Dynamic characteristics curves of θ_1; (b) Dynamic characteristics curves of ψ_1; (c) Dynamic characteristics curves of θ_2; (d) Dynamic characteristics curves of ψ_2.

(a)
          (b)

(c)
          (d)
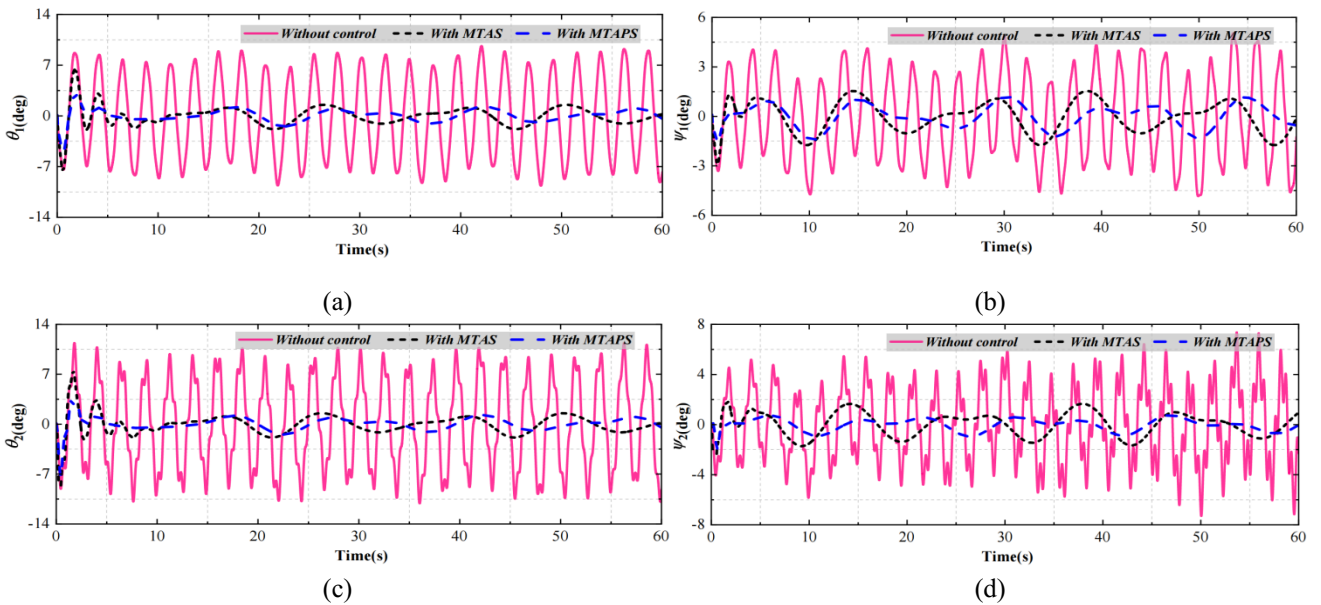
Fig. 9 Contrastive analysis with and without anti-swing under sea state 5. (a) Dynamic characteristics curves θ_1; (b) Dynamic characteristics curves of ψ_1; (c) Dynamic characteristics curves of θ_2; (d) Dynamic characteristics curves of ψ_2.

(a)
          (b)
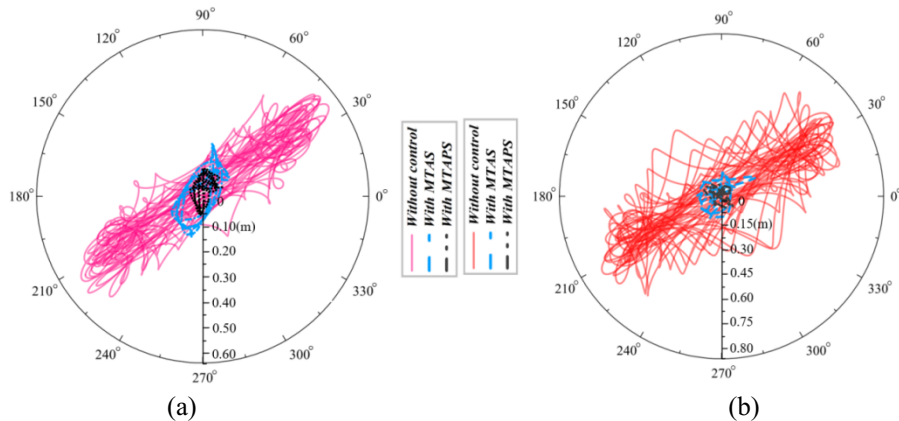
Fig. 10 Comparison of projection area with and without anti-swing system. (a) Comparison of projection area under sea state 4; (b) Comparison of projection area under sea state 5.

Table. 2 Comparison of anti-swing effects between MTAS and MTPAS

Case	Angle type	Without control/°	With MTAS/°	With MTAPS/°	Pendulum reduction ratio/(%)	Average swing angle reduction ratio/(%)	Projected area reduction ratio/(%)
Sea state 4	θ_1	6.52	1.42	0.95	78/85	74/83	71/82
	ψ_1	2.8	0.72	0.54	74/81		
	θ_2	7.59	1.72	1.1	76/85		
	ψ_2	3.3	1.02	0.59	69/82		
Sea state 5	θ_1	9.7	1.91	1.3	80/86	76/85	72/84
	ψ_1	4.3	1.16	0.86	72/80		
	θ_2	10.4	1.89	0.94	81/90		
	ψ_2	5.9	1.71	0.82	71/86		

4.2 Dynamics analysis of the MTAS and the MTPAS

To investigate the suppression effect of the ASPD on the double swing of the SBP, simulations were conducted to analyze the length ratio of the hoist tagline to the SBP and the mass ratio of the ASPD to the SBP in the double-pendulum system. For simplicity, these ratios are denoted as $L=L_1/L_2$ and $R=m_1/m_2$, respectively, with the initial swing angle of the SBP set to 15°. **Fig. 11** illustrates the relationship between the stability time and variations in L under sea states 4 and 5. When the length of the SBP exceeds that of the hoist tagline (i.e., L decreases), the stability time of the system with the ASPD is significantly shorter than that without the ASPD, due to the effective transfer of binding force by the ASPD, which reduces the swing in the double-pendulum system. Conversely, when the SBP length is less than that of the hoist tagline (i.e., L increases), the influence of the ASPD on the double-pendulum system diminishes. As the length of the hoist tagline increases, so too does the length of the anti-swing taglines, which in turn weakens the component forces in the x and y directions, resulting in diminished anti-swing performance.

(a)   (b)

(c)

(d)
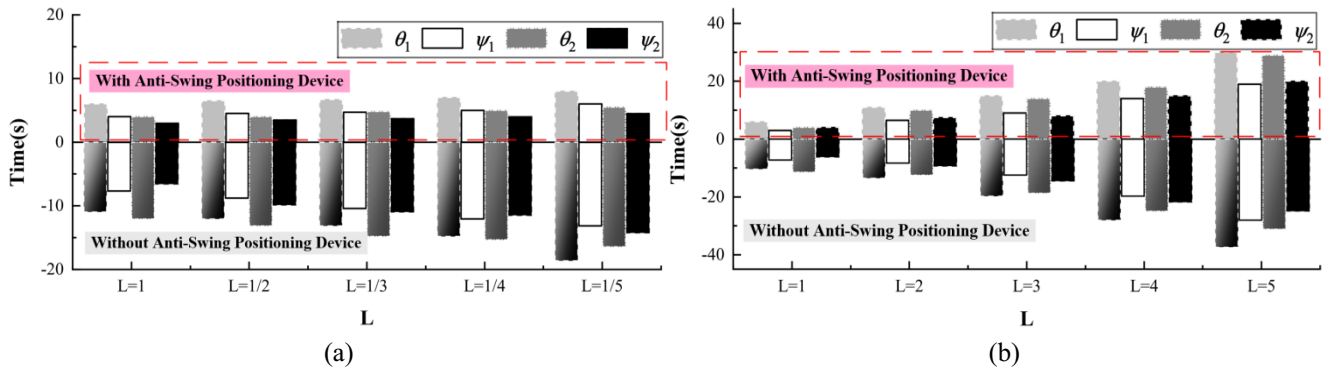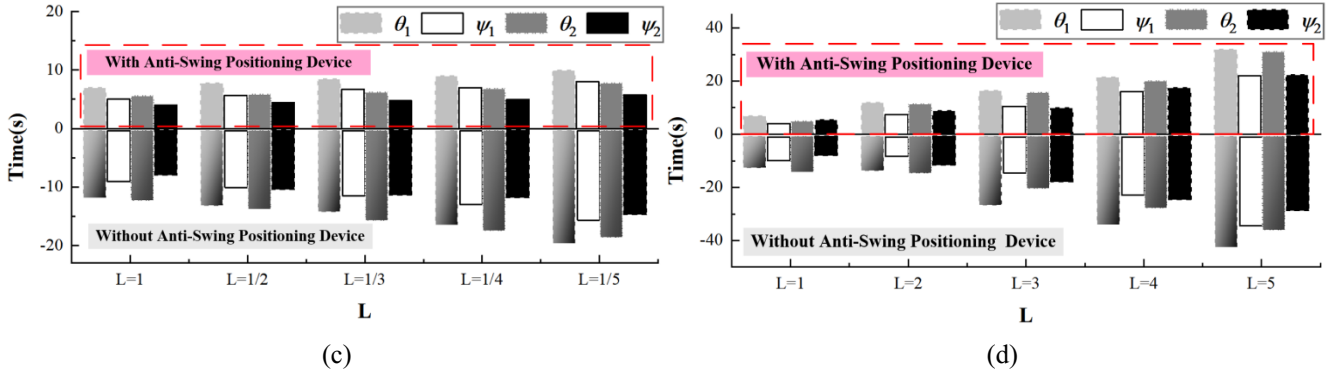
Fig. 11 Effect of length ratio on the system (a) *L* decreasing scenario under sea state 4; (b) *L* increasing scenario under sea state 4; (c) *L* decreasing scenario under sea state 5; (b) *L* increasing scenario under sea state 5

As shown in **Fig. 12**, when the mass of the SBP exceeds that of the ASPD (i.e., *R* decreases), the stability time of the double-pendulum system with the ASPD is notably shorter than without it. This indicates that the ASPD can effectively suppress the motion of the double-pendulum as the SBP mass increases. However, when the SBP mass is less than that of the ASPD (i.e., *R* increases), the ASPD's influence is less pronounced. Simulation analysis reveals that as the mass or length of the SBP in the double-pendulum system increases, the ASPD effectively transmits the binding force of the anti-swing taglines to the SBP, thereby suppressing system motion. Nevertheless, when the length of the anti-swing taglines becomes excessive, the component forces in the *x* and *y* directions are insufficient, reducing the anti-swing effectiveness on the SBP. This finding suggests that the MTAPS may not be suitable for scenarios involving long tagline lengths, such as underwater lifting operations.

(a)

(b)
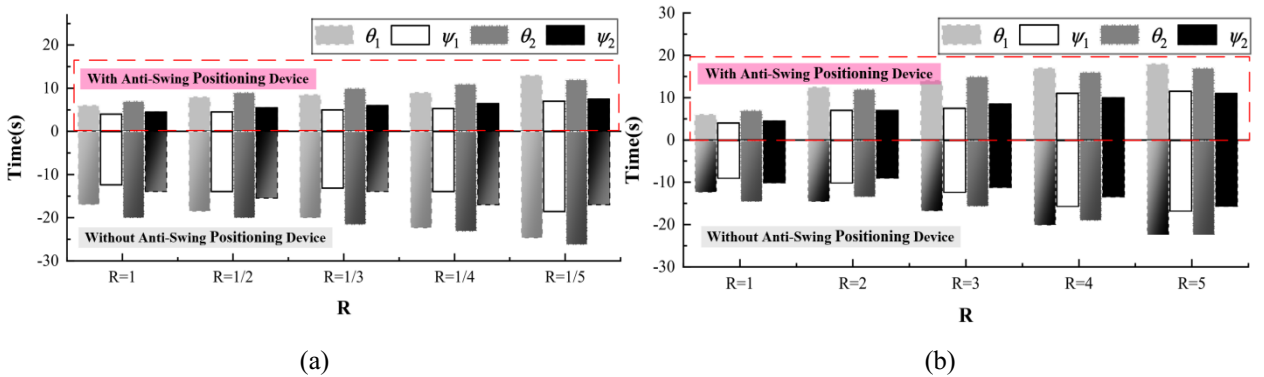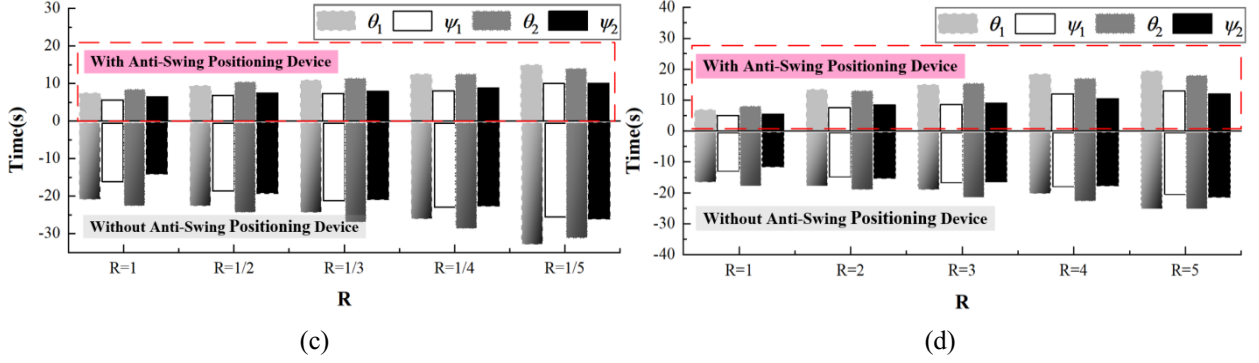
Fig. 12 Effect of mass ratio on the system (a) *R* decreasing scenario under sea state 4; (b) *R* increasing scenario under sea state 4; (c) *R* decreasing scenario under sea state 5; (b) *R* increasing scenario under sea state 5

4.3 Nonsingular fast terminal sliding-mode control

We developed a Nonsingular Fast Terminal Sliding-Mode Control (NFTSMC) for the MTAPS to improve its anti-swing capabilities during the lifting of a SBP. Using a second-order system as an example, we formulated the control law and validated the system's stability using Lyapunov theory.

Let define the error $e_1 = y - y_d$ and its derivative $e_2 = \dot{y} - \dot{y}_d$ where $\dot{y}_d$ is the reference signal. The system error is then be redefined as

$$\begin{aligned} \dot{e}_1 &= e_2 \\ \dot{e}_2 &= F(\chi) + D(\chi,t) + B(\chi)\tau(t) \end{aligned} \tag{53}$$

$D(\chi,t) = \Delta f(\chi) + d(t)$ represents the lumped uncertainty of the system.

The uncertainties $\Delta f(\chi)$ and the external disturbances $d(t)$ are unknown and assumed to be bounded by a positive as follows

$$|D(\chi,t)| = |\Delta f(\chi) + d(t)| \le \delta \tag{54}$$

An NFTSM surface σ(*t*) is introduced as follows.

$$\sigma(t) = e_1 + k_1 |e_1|^{\alpha} sign(e_1) + k_2 |e_2|^{\beta} sign(e_2) \tag{55}$$

Where k_1 and k_2 are positive numbers, $1 < \beta < 2$ and $\alpha > \beta$.

Substituting Eq. (53) into the differentiated form of Eq. (55), we can obtain

$$\dot{\sigma}(t) = e_2 + \alpha.k_1 |e_1|^{\alpha-1} e_2 + \beta.k_2 |e_2|^{\beta-1} (F(\chi) + B(\chi)\tau) \tag{56}$$

When $\dot{\sigma} = 0$, the equivalent control law is derived as:

$$\tau_{eq}(t) = B^{-1}(\chi)\left[-F(\chi) - \frac{1}{\beta.k_2} |e_2|^{2-\beta} (1 + \alpha.k_1 |e_1|^{\alpha-1}) sign(e_2) \right] \tag{57}$$

To enhance the robustness of the controller, a switching control law is further proposed.

$$\tau_{sw}(t) = B^{(-1)}(\chi) * [-k.\sigma - \eta sign(\sigma)] \tag{58}$$

where $\eta>0$ is a small positive constant and $k>0$ is the switching gain, a_0, a_1 and a_2 are positive numbers. Then the overall control law can be expressed as:

$$\tau(t) = \tau_{eq}(t) + \tau_{sw}(t)$$
$$= B^{-1}(\chi) * [-F(\chi) - \frac{1}{\beta.k_2} |e_2|^{2-\beta} (1 + \alpha.k_1 |e_1|^{\alpha-1}) sign(e_2) - k.\sigma - \eta sign(\sigma)] \quad (59)$$

Lyapunov function of sliding mode control is written:

$$V = \frac{1}{2}\sigma^2 \quad (60)$$

$$\dot{V} = \sigma\dot{\sigma} = \sigma(e_2 + \alpha.k_1 |e_1|^{\alpha-1} e_2 + \beta.k_2 |e_2|^{\beta-1} \dot{e}_2) \quad (61)$$

By substituting Eq. (53) and (59) into Eq. (61), the derivative of V can be rewritten as:

$$\dot{V} = \beta.k_2 |e_2|^{\beta-1} [D(\chi,t)\sigma - k\sigma^2 - (\delta+\eta)|\sigma|] \quad (62)$$

It is straightforward to verify that

$$\dot{V} \le \beta.k_2 |e_2|^{\beta-1} [|D(\chi,t)|.|\sigma| - k\sigma^2 - (\delta+\eta)|\sigma|]$$
$$= \beta.k_2 |e_2|^{\beta-1} [(|D(\chi,t)| - \delta).|\sigma| - k\sigma^2 - \eta|\sigma|] \quad (63)$$

From Eq. (54), it can be concluded that

$$\dot{V} \le \beta.k_2 |e_2|^{\beta-1} [k\sigma^2 - \eta|\sigma|] \le 0 \quad (64)$$

According to the Lyapunov stability theory, the system gradually converges to the surface $\sigma(t)=0$. To prove that the convergence occurs within finite time, Eq. (64) can be rewritten as

$$\dot{V} = \frac{dV}{dt} \le -2\beta.k.k_2 |e_2|^{\beta-1} V - \beta.k_2.\eta |e_2|^{\beta-1} \sqrt{2}V^{1/2} = -\rho_1 V - \rho_2 V^{1/2} \quad (65)$$

where $\rho_1 = 2\beta.k.k_2 |e_2|^{\beta-1} > 0$ and $\rho_2 = \beta.k_2\eta |e_2|^{\beta-1} \sqrt{2} > 0$

Further calculations yield

$$dt \le \frac{-dV}{\rho_1 V + \rho_2 V^{1/2}} = \frac{-V^{-1/2}dV}{\rho_1 V^{1/2} + \rho_2} = -2\frac{dV^{1/2}}{\rho_1 V^{1/2} + \rho_2} \quad (66)$$

Suppose that the reaching time from the initial state $e(0) \ne 0$ to $e=0$ is t_r, that is, $V(t_r)=0$. By integrating both sides of equation (66), we have

$$\int_0^{t_r} dt \le \int_0^{t_r} \frac{-2.dV^{1/2}}{\rho_1 V^{1/2} + \rho_2} = \left[\frac{-2}{\rho_1} \ln(\rho_1 V^{1/2} + \rho_2)\right]_{V(0)}^{V(t_r)} \quad (67)$$

$$t_r \le \frac{2}{\rho_1} \ln(\frac{\rho_1 V(0)^{1/2} + \rho_2}{\rho_2}) \quad (68)$$

According to the Lyapunov stability theory, the NFTSMC surface $\sigma(t)$ in Eq. (55) will converge to zero within a finite time, as shown in Eq. (68). Furthermore, if $\sigma(t)=0$, the system's output error will also converge to zero within a finite time, thus completing the proof.

In conjunction with the dynamic model in Section 3.2, based on the previous derivation, the sliding surfaces s_1 and s_2 can be expressed as follows

$$s_1 = e_1 + k_1 |e_1|^\alpha \sin gn(e_1) + k_2 |e_1|^\beta \sin gn(e_1) \tag{69}$$

$$s_2 = e_2 + k_1 |e_2|^\alpha \sin gn(e_2) + k_2 |e_2|^\beta \sin gn(e_2) \tag{70}$$

The controller design for the anti-sway system is as follows

$$f_x = (1/F(\chi_\theta))(-B(\chi_\theta) - (1/(k_2\beta))|e_1|^{2-\beta} sign(e_1)(1 + k_1 |e_1|^{\alpha-1})) - 20s_1 - \eta sign(s_1)) \tag{71}$$

$$f_y = (1/F(\chi_\psi))(-B(\chi_\psi) - (1/(k_2\beta))|e_2|^{2-\beta} sign(e_2)(1 + k_1 |e_2|^{\alpha-1})) - 20s_2 - \eta sign(s_2)) \tag{72}$$

where $\alpha=2$, $\beta=5/3$, $k_1=0.2$, $k_1=0.5$, $k=6$, $\eta=4$. $F(\chi)$ can be expressed as

$$F(\chi_\theta) = \cos\theta_1 \tan\psi_1 / m_1 L_1 \sin\psi_1 \tag{73}$$

$$F(\chi_\psi) = (\sin\theta_1^2 + \cos\theta_1^2) / m_1 L_1 (\cos\psi_1 + \sin\psi_1 \tan\psi_1) \tag{74}$$

$B(\chi)$ can be expressed as

$$B(\chi_\theta) = (\sin\theta_1(\cos\theta_1(F_{Ky} - m_1(-L_1\dot\psi_1^2 \sin\psi_1)) - \tan\psi_1(-f_z + F_{Kz} + m_1 g + m_1(L_1 \cos\theta_1 \cos\psi_1(\dot\theta_1^2 + \dot\psi_1^2)$$
$$-2L_1\dot\theta_1\dot\psi_1 \sin\theta_1 \sin\psi_1))) - \cos\theta_1(\sin\theta_1(F_{Ky} - m_1(-L_1\dot\psi_1^2 \sin\psi_1)) - \tan\psi_1(F_{Kx} - m_1(-2L_1\dot\theta_1\dot\psi_1 \cos\theta_1 \sin\psi_1 \tag{75}$$
$$-L_1 \sin\theta_1 \cos\psi_1(\dot\theta_1^2 + \dot\psi_1^2))))) / m_1 L_1 \sin\psi_1$$

$$B(\chi_\psi) = (\sin\theta_1(\sin\theta_1(F_{Ky} - m_1(-L_1\dot\psi_1^2 \sin\psi_1)) - \tan\psi_1(F_{Kx} - m_1(-2L_1\dot\theta_1\dot\psi_1 \cos\theta_1 \sin\psi_1 - L_1 \sin\theta_1 \cos\psi_1(\dot\theta_1^2 + \dot\psi_1^2))))$$
$$+\cos\theta_1(\cos\theta_1(F_{Ky} - m_1(-L_1\dot\psi_1^2 \sin\psi_1)) - \tan\psi_1(-f_z + F_{Kz} + m_1 g + m_1(L_1 \cos\theta_1 \cos\psi_1(\dot\theta_1^2 + \dot\psi_1^2) - 2L_1\dot\theta_1\dot\psi_1 \sin\theta_1 \sin\psi_1)))) \tag{76}$$
$$/m_1 L_1 (\cos\psi_1 + \sin\psi_1 \tan\psi_1)$$

As shown in **Fig. 13**, we conducted a comparative analysis of the anti-swing performance of three control methods—MTAS, MTAPS, and NFTSMC—on a double-pendulum system for SBP under sea state 5. **Tab. 3** summarizes the simulation data, the simulation results demonstrate that all three methods effectively reduce swing in the double-pendulum system. Among them, NFTSMC proves to be superior, enabling the system to reach a relatively stable state more quickly. Compared to MTAPS, NFTSMC improves the average swing angle reduction ratio by approximately 11%, proving its enhanced anti-swing performance for lifting SBP.

(a)　　　　　　　　　　　　　　(b)

(c)   (d)
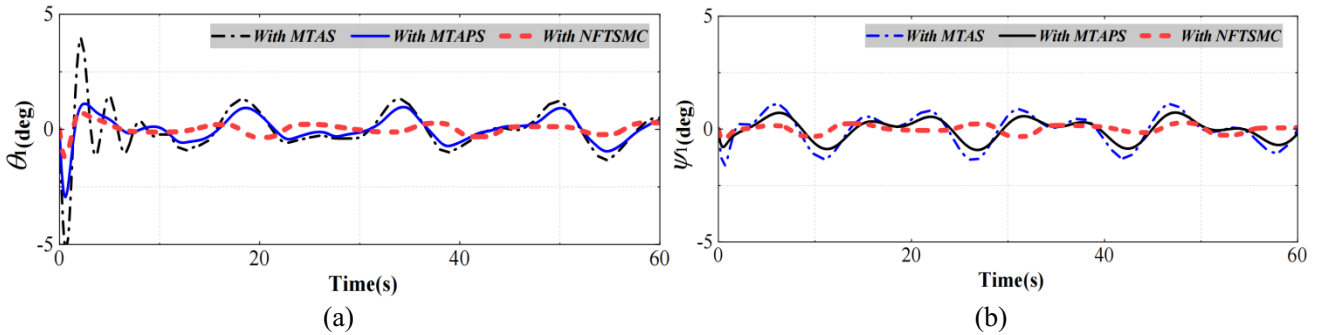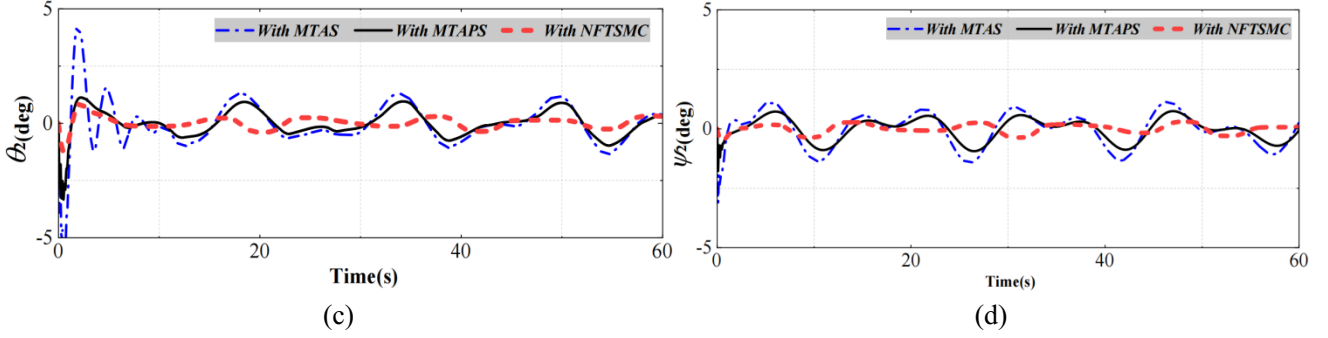
Fig. 13 Comparative analysis of different control methods under sea state 5. (a) Dynamic characteristics curves θ_1; (b) Dynamic characteristics curves of ψ_1; (c) Dynamic characteristics curves of θ_2; (d) Dynamic characteristics curves of ψ_2.

Table. 3 Comparison of anti-swing effects using three control methods

Case	Angle type	With MTAS/°	With MTAPS/°	With NFTSMC/°	Pendulum reduction ratio/(%)	Average swing angle reduction ratio/(%)
	θ_1	1.91	1.3	0.48	80/86/95	
	ψ_1	4.3	0.86	0.36	72/84/92	
Sea state 5						74/83/94
	θ_2	10.4	0.94	0.42	81/90/97	
	ψ_2	5.9	0.82	0.34	71/84/94	

5 Experiment verification

As illustrated in **Fig. 15**, the experimental prototype consists of a crane prototype and a Stewart platform (150 cm long × 150 cm wide × 140 cm high). The telescopic variation range of the main jib of the crane prototype is 1.5 m to 2.1 m. The dimensions of the experimental prototype for the multi-tagline anti-swing system are: L_{OK}=1.4 m, L_{OH}=1.8 m, L_{OD}=1.9 m, L_{OE}=2.1 m, L_{EF}=2.1 m, L_{HN}=L_{HN}=1.0 m, L_{OA}=0.7 m, θ_{2y}=60°. The anti-swing payload device (ASPD) is constructed from lightweight aluminum alloys and plastics, weighing 6 kg. The SBP has a length of 1 m and a mass of 10 kg. The hoist tagline measures 1.2 m during lifting experiments. Experiments were conducted on both regular payloads and the SBP, using the experimental prototype. It is important to note that the sway reduction effect of the anti-swing system on both regular payloads and the SBP is influenced by factors such as the sea state level, the length of the hoist tagline, the mass of the regular payload, and the dimensions and mass of the SBP.

5.1 The electronic control system of the MTAS

Fig. 14 illustrates the layout scheme of the electronic control system for the anti-swing crane prototype. This system comprises a control system, a power system, and a measurement system. Four anti-swing motors, each equipped with an encoder, are mounted at the rear of the crane's main

jib to measure the length variations of the anti-swing taglines. Tension sensors are positioned near the motor drums to monitor the tension in these taglines. Additionally, two encoders are installed perpendicular to each other at the end of the main jib to measure the in-plane and out-of-plane angles of the payload. A tilt sensor is utilized to gauge the swing angle of the SBP. The electronic control system collects signals from each sensor in real-time and relays this information to the PLC. After processing the data, the PLC generates control signals that drive the motors, thus controlling the four anti-swing taglines to mitigate the swing of the payload.
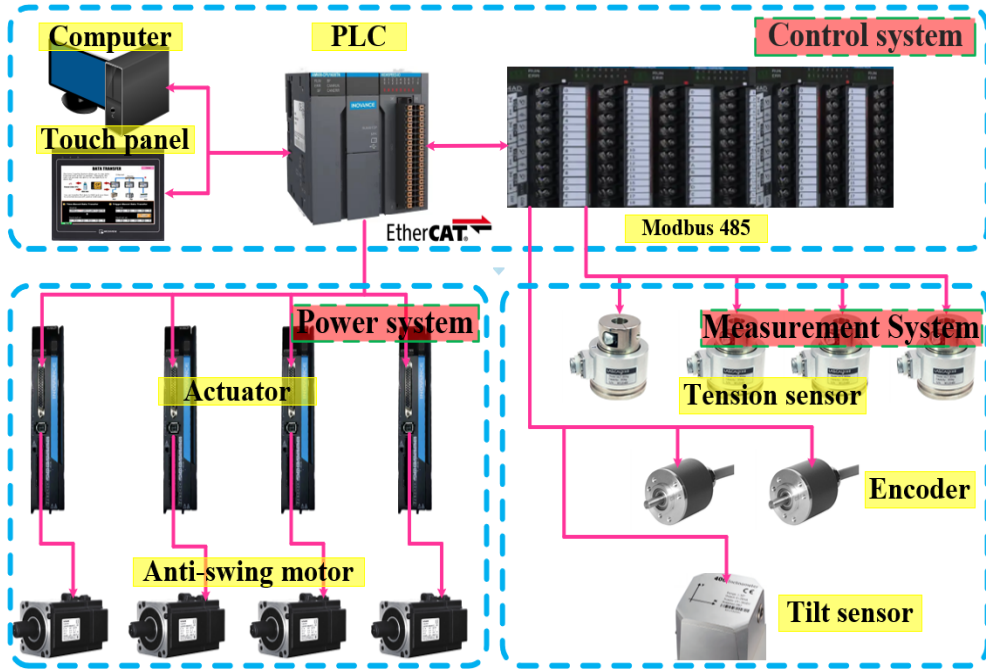
Fig. 14 Electrical control logic diagram of the MTAS

As depicted in **Fig. 15**, the crane experiment prototype equipped with the MTAPS includes the following components: 1, 2-electrical control system; 3, 4-Stewart platform and control system; 5-crane prototype, the MTAS, and the ASPD; 6-SBP. The Stewart platform simulates ship movements under various sea conditions. The MTAPS configuration comprises four anti-swing taglines, anti-swing jibs, motors, various sensors, and electrical systems. Anti-swing taglines I and IV manage the swing of the payload in the in-plane direction, whereas taglines II and III control the out-of-plane swing. This mechanical arrangement facilitates the decoupling control of the payload's swing. The ASPD primarily consists of multi-link gripping clips, lead screws, stepper motors, sliders, and an anti-swing platform. In conjunction with the MTAS, the ASPD manipulates the MTAPS, controlling the movement through multiple anti-swing taglines and transmitting the binding force to the SBP via mechanical components like the multi-link gripping clip, thereby allowing the MTAPS to suppress the swing of the SBP in any direction. Following the tension setting method outlined in Eq. (52), the tensions and their thresholds post-calibration are set as follows: $F_{1s}=F_{4s}=30N$, $\delta_1=\delta_4=15N$,

$F_{2s}=F_{3s}=25N$, $\delta_2=\delta_3=12N$.. Experiments were performed to validate the efficacy of the anti-swing system.
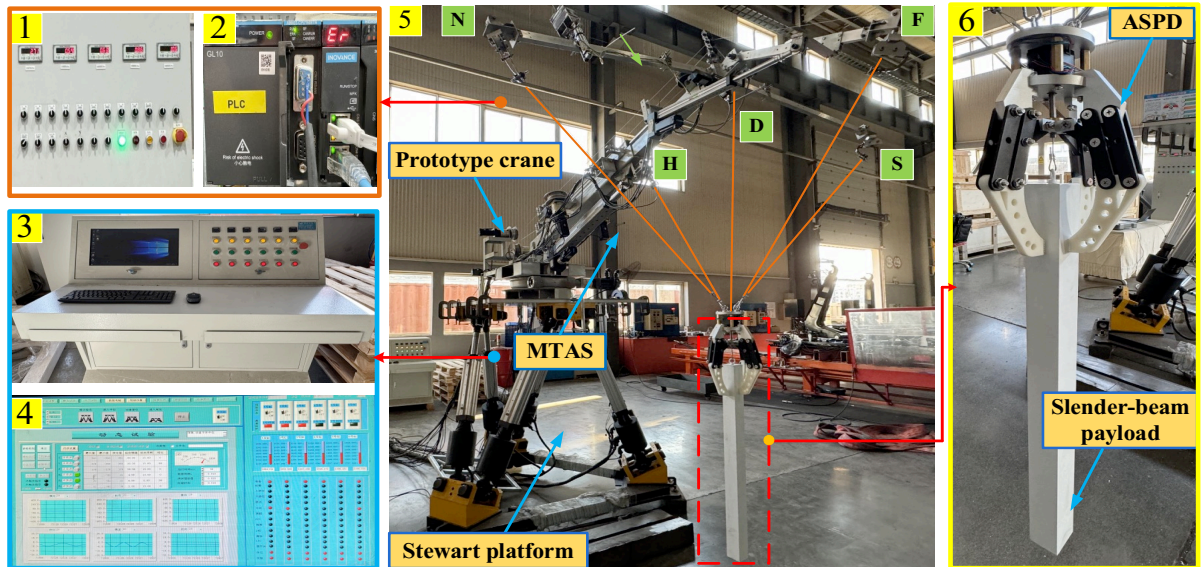
Fig. 15 Experimental drawing of the MTAPS for lifting the SBP

5.2 Comparative experiment on sway reduction with regular payload

Two sets of experiments were conducted on the Stewart platform to evaluate the performance of the anti-swing system. Ship-motion excitation were set to $\theta_{1x}=4\sin(\pi t/3)$, $\theta_{1y}=3\sin(\pi t/5)$ for the first set (referred as Condition 1) and $\theta_{1x}=6\sin(\pi t/4)$, $\theta_{1y}=4\sin(\pi t/6)$ for the second set (Condition 2). **Fig. 16** shows the experimental results for the anti-swing experiments under these two conditions, while **Fig. 17** shows the projected trajectory of the regular payload on the horizontal plane, allowing for the determination of the projected area. **Tab. 4** compiles the data from the two sets of anti-swing experiments. The average swing angle reduction ratio of the MTAS for the regular payload under conditions 1 and 2 is 91.4% and 90.2%, respectively. The reduction ratio of the projected area is 96.8% and 95.6%, respectively. The experimental results indicate that the MTAS is highly effective in reducing the of the payload when subjected to ship-motion excitation circumstances.

(a)

(b)

(c)

(d)
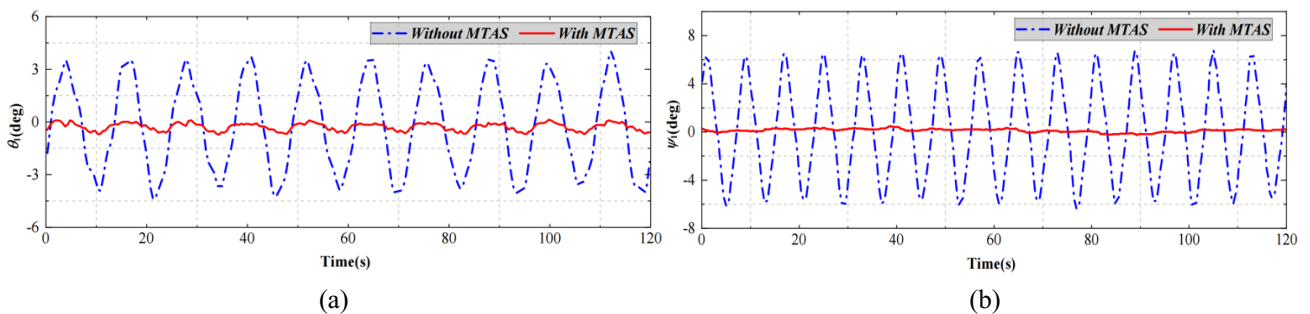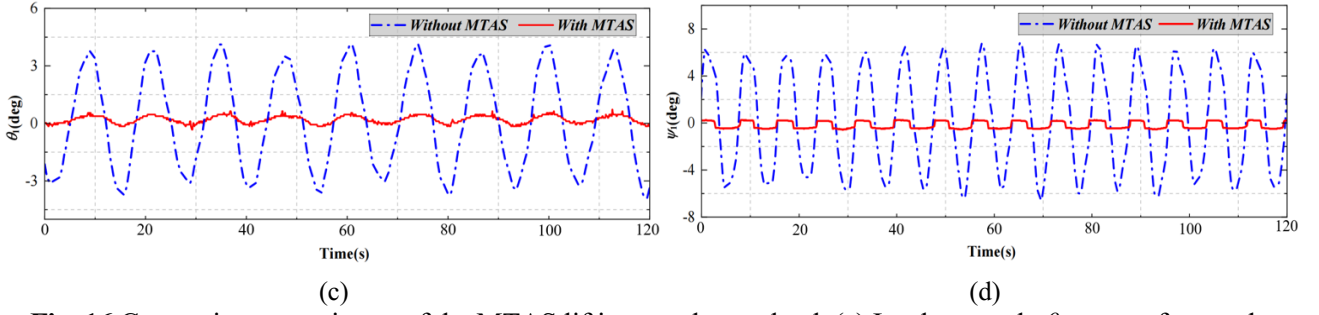
Fig. 16 Comparison experiment of the MTAS lifting regular payload. (a) In-plane angle θ_1 curves for regular payload under condition 1; (b) Out-plane angle ψ_1 curves for regular payload under condition 1; (c) In-plane angle θ_1 curves for regular payload under condition 2; (d) Out-plane angle ψ_1 curves for regular payload under condition 2.

(a)

(b)
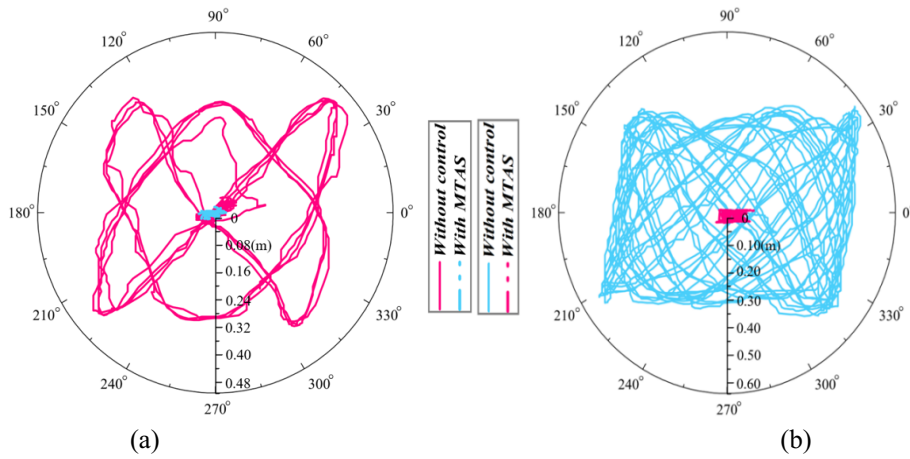
Fig. 17 The projected area of the regular payload. (a) Comparison of projection area under Condition 1; (b) Comparison of projection area under Condition 2.

Table. 4 Results of the anti-swing experiment of the regular payload

Case	Angle type	Without control/°	With control/°	Pendulum reduction ratio/(%)	Average swing angle reduction ratio/(%)	Projected area reduction ratio/(%)
Condition 1	θ_1	3.6	0.49	86.4	91.4	96.8
	ψ_1	6.5	0.24	96.3		
Condition 2	θ_1	4.15	0.65	84.3	90.2	95.6
	ψ_1	7.1	0.37	94.8		

To explore the relationship between the swing angle and the tension in the hoist tagline, these variables were plotted over the same time interval. **Figs. 18** and **19** illustrate that θ_1 denotes the in-plane angle of the hoist tagline, with the direction toward point F defined as positive. The trend in the tension of anti-swing tagline I generally corresponds with that of the in-plane angle of the hoist tagline. In contrast, the trend in the tension of anti-swing tagline IV is inverse to that of the in-plane angle. The experimental curves reveal that as the payload swings toward point F, the tension in anti-swing tagline I progressively increases, whereas the tension in anti-swing tagline IV steadily decreases. This pattern suggests that anti-swing tagline I absorbs the swing energy of the payload,

while anti-swing tagline IV merely maintains sufficient tension to prevent slack. Conversely, when the payload swings toward point K, anti-swing tagline IV absorbs the swing energy, and anti-swing tagline I simply maintains tension. This dynamic is similarly applicable in explaining the variations in the out-of-plane angle (ψ_1) of the payload and the tensions in the anti-swing taglines. As depicted in **Figs. 18** and **19**, the tension in all four anti-swing taglines remains positive and within the predefined limits, corroborating the validity of Eq. (51). Thus, regardless of the swinging direction of the payload, the tension in all four anti-swing taglines consistently acts to impede the payload's motion.
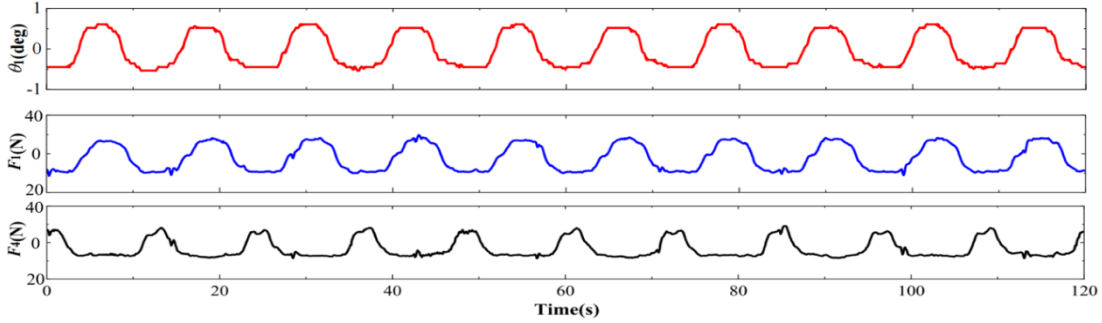
Fig. 18 Experimental contrast curve of in-plane angle and tagline tension
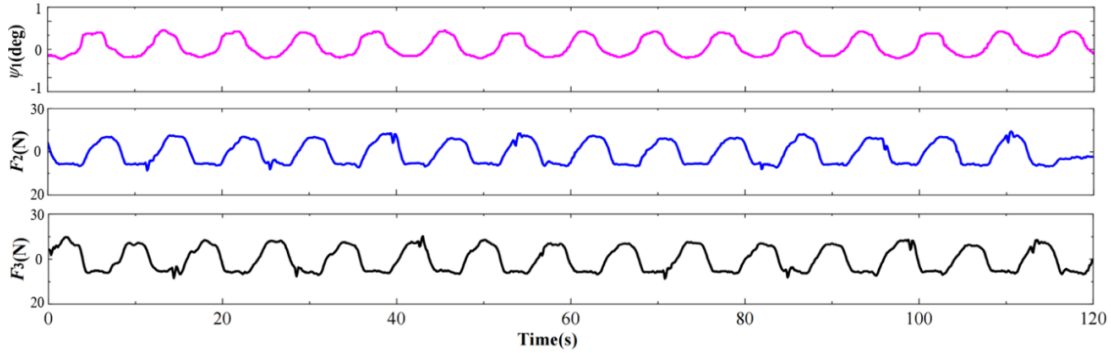
Fig. 19 Experimental results of out-of-plane angle and tagline tension

5.3 Comparative experiment on sway reduction with SBP

Figs 20 and **21** depict the experiments conducted on lifting the SBP using the MTAPS under Condition 1. These experiments demonstrate that the average swing angle reduction ratio at the primary swing angle is 88%, while at the secondary swing angle, it is 83%. The anti-swing effect of the system on the SBP proved slightly less effective compared to its effect on a regular payload. This discrepancy is attributed to the interaction forces between the SBP and the MTAPS, which cause irregularities in the secondary swing angle. The experimental data, summarized in **Tab. 5**, indicate that the average swing angle reduction ratio exceeds 85% and the projected area reduction ratio surpasses 86%. These results confirm the efficacy of the MTAPS in reducing the swing of the SBP under ship-motion excitation.
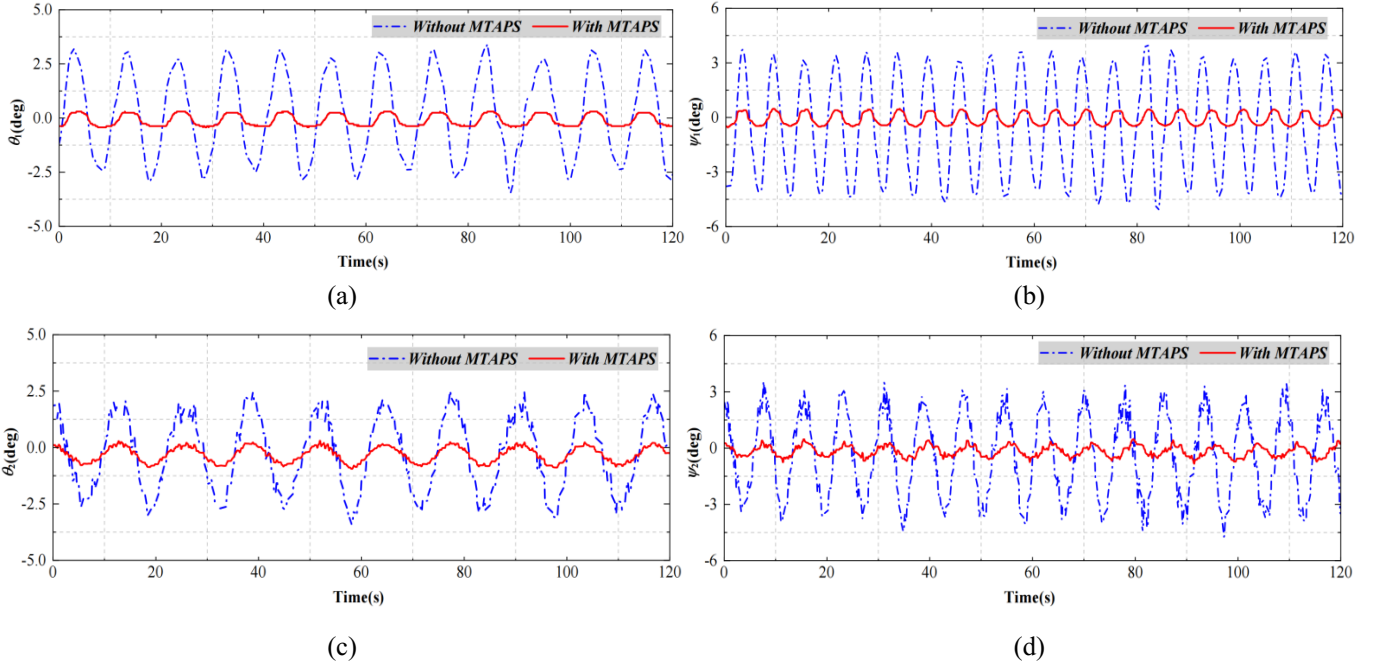
Fig. 20 Comparison experiment of the MTAPS lifting the SBP under Condition 1. (a) In-plane angle θ_1 curves for the hook; (b) Out-plane angle ψ_1 curves for the hook; (c) In-plane angle θ_2 curves for the SBP; (d) Out-plane angle ψ_2 curves for the SBP.
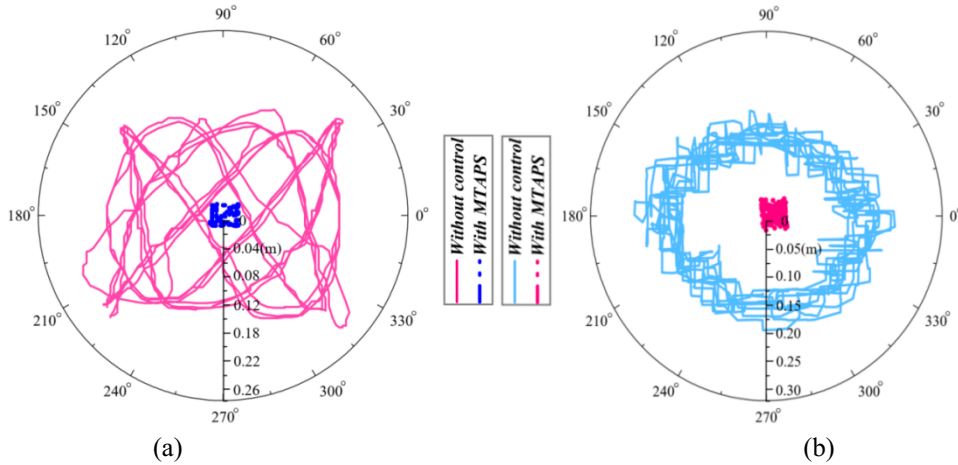
Fig. 21 The projected area of the MTAPS. (a) Comparison of projection area of the hook; (b) Comparison of projection area of the SBP.

Table. 5 Results of the anti-swing experiment of the SBP

Case	Angle type	Without control/°	With control/°	Pendulum reduction ratio/(%)	Average swing angle reduction ratio/(%)	Projected area reduction ratio/(%)
Condition 1	θ_1	3.3	0.35	89	85	86
	ψ_1	3.9	0.5	87		
	θ_2	2.8	0.46	84		
	ψ_2	3.7	0.68	82		

6 Conclusion

In this study, we introduce a novel MTAPS designed for lifting the SBP under challenging sea conditions. A dynamic model of a 3D double-pendulum system is developed, employing multi-body dynamics and Newtonian mechanics. We compare the anti-swing performance and dynamic characteristics of the MTAS and the MTAPS in lifting the SBP under ship-motion excitation. The effectiveness of the anti-swing system for both a regular payload and the SBP has been rigorously evaluated through experimental testing.

(1) The pendulum reduction ratios for the MTAS and the MTAPS are 74% and 83%, respectively, with projected area reduction ratios of 71% and 82%, respectively, under sea state 4. The MTAPS's anti-swing positioning device effectively transfers the binding force from multiple anti-swing taglines directly to the SBP through a multi-link gripping clip.

(2) When compared to the MTAS, the MTAPS significantly reduces the time required for the double-pendulum system to achieve relative stability, particularly when lifting heavier and longer SBP. This enhancement enables marine cranes to perform rapid transfers and precise positioning of the SBP during offshore lifting operations.

(3) Experimental data indicate that the average swing angle reduction ratio and the projected area reduction ratio of the MTAS for a regular payload are above 90% and 95%, respectively, under specified working conditions. For the MTAPS, these ratios for the SBP are above 85%. The results, derived from comprehensive hardware trials, conclusively demonstrate that the anti-swing system effectively mitigates swaying for both the regular payload and the SBP.

These findings underscore the potential of the MTAPS for vertical lifting and transferring tasks involving the SBP, including but not limited to, deploying and retrieving buoys, lifting wind turbines, and installing wind turbine towers. Additionally, this study contributes new methods to model the structural and dynamic responses of MTAPSs, providing fresh insights into the design of multi-tagline offshore anti-swing cranes.

Further work

Future research will concentrate on the development of a nonlinear controller for the MTAPS, including enhancements to multi-tagline systems and the ASPD, to further improve the anti-swing capabilities of the system. We will also extend our investigations to address anti-swing and anti-slip issues comprehensively throughout the entire process, from single-point lifting to free suspension, in double-pendulum systems such as the SBP.

Statements & Declarations

References

Aksjonov, A., Vodovozov, V., Petlenkov, E., 2015. Three-Dimensional Crane Modelling and Control Using Euler-Lagrange State-Space Approach and Anti-Swing Fuzzy Logic. Electrical Control and Communication Engineering 9 (1), 5-13.

Baillieul, J., 1987. Introduction to ROBOTICS mechanics and control. IEEE Transactions on Automatic Control 32 (5), 463-464.

Ben Hazem, Z., Fotuhi, M.J., Bingül, Z., 2020. Development of a Fuzzy-LQR and Fuzzy-LQG stability control for a double link rotary inverted pendulum. Journal of the Franklin Institute-Engineering and Applied Mathematics 357 (15), 10529-10556.

Ben Hazem, Z., Fotuhi, M.J., Bingül, Z., 2022. Anti-swing radial basis neuro-fuzzy linear quadratic regulator control of double link rotary pendulum. Proceedings of the Institution of Mechanical Engineers Part I-Journal of Systems and Control Engineering 236 (3), 531-545.

Blackburn, D., Singhose, W., Kitchen, J., Patrangenaru, V., Lawrence, J., Kamoi, T., Taura, A., 2010. Command Shaping for Nonlinear Crane Dynamics. Journal of Vibration and Control 16 (4), 1-25.

Cao, Y.C., Li, T.S., 2024. Nonlinear antiswing control for shipboard boom cranes with full state constraints. Applied Ocean Research 146.

Cibicik, A.E., Olav, 2019. Dynamic modelling and force analysis of a knuckle boom crane using screw theory. Mechanism and Machine Theory: Dynamics of Machine Systems Gears and Power Trandmissions Robots and Manipulator Systems Computer-Aided Design Methods 133.

Fatehi, M.H., Eghtesad, M., Amjadifard, R., 2014. Modelling and Control of an Overhead Crane System with a Flexible Cable and Large Swing Angle. Journal of Low Frequency Noise Vibration and Active Control 33 (4), 395-409.

Fossen, T.I., 1994. Guidance and control of ocean vehicles. Guidance and control of ocean vehicles.

Ham, S.H., Roh, M.I., Kim, J.S., 2018. Numerical analysis of wreck removal based on multibody system dynamics. Journal of Marine Science and Technology 23 (3), 521-535.

Hazem, Z.B., Fotuhi, M.J., Bingül, Z., 2023. A Study of Anti-swing Fuzzy LQR Control of a Double Serial Link Rotary Pendulum. Iete Journal of Research 69 (6), 3443-3454.

Huang, J., Liang, Z., Zang, Q., 2015. Dynamics and swing control of double-pendulum bridge cranes with distributed-mass beams. Mechanical Systems and Signal Processing 54, 357-366.

Huang, J., Xie, X., Liang, Z., 2014. Control of Bridge Cranes With Distributed-Mass Payload Dynamics. IEEE/ASME Transactions on Mechatronics 20 (1), 481-486.

Hussein, E.Q., Al-Dujaili, A.Q., Ajel, A.R., 2020. Design of sliding mode control for overhead crane systems, IOP Conference Series: Materials Science and Engineering. IOP Publishing, p. 012084.

Jaafar, H., Mohamed, Z., Shamsudin, M., Subha, N.M., Ramli, L., Abdullahi, A., 2019. Model reference command shaping for vibration control of multimode flexible systems with application to a double-pendulum overhead crane. Mechanical Systems and Signal Processing 115, 677-695.

Kimiaghalam, B., Homaifar, A., Bikdash, M., 2000. Feedback and feedforward control law for a ship crane with Maryland rigging system, American Control Conference.

Ku, N.K., Cha, J.H., Roh, M.I., Lee, K.Y., 2013. A tagline proportional-derivative control method for the anti-swing motion of a heavy load suspended by a floating crane in waves. Proceedings of the Institution of Mechanical Engineers Part M Journal of Engineering for the Maritime Environment 227 (4), 357-366.

Lee, H.H., Liang, Y., Segura, D., 2006. A sliding-mode antiswing trajectory control for overhead cranes with high-speed load hoisting. Journal of Dynamic Systems Measurement and Control-Transactions of the Asme 128 (4), 842-845.

Love, L., 2003. Compensation of Wave-Induced Motion and Force Phenomena for Ship-Based High Performance Robotic and Human Amplifying Systems. Office of Scientific & Technical Information Technical Reports.

Maleki, E., Singhose, W., 2012. Swing Dynamics and Input-Shaping Control of Human-Operated Double-Pendulum Boom Cranes. Journal of Computational and Nonlinear Dynamics 7 (3).

Martin, I.A., Irani, R.A., 2021. Dynamic modeling and self-tuning control of a seven degree of freedom shipboard knuckle boom crane. Mechanical Systems and Signal Processing 153 (4), 107441.

McTaggart, K., de Reilhac, P.R., Boudet, L., Oakey, S., 2019. Validation of a distributed simulation of ship replenishment at sea with model tests. Journal of Marine Science and Technology 24 (4), 1209-1222.

Parker, G., Graziano, M., Leban, F., Green, J., Bird, J.D., Ieee, 2007. Reducing crane payload swing using a rider mock tagline control system, Oceans 2007 Europe International Conference, Aberdeen, SCOTLAND, pp. 1118-+.

Renuka, V.S., Mathew, A.T., 2013. Precise Modelling of a Gantry Crane System Including Friction, 3D Angular Swing and Hoisting Cable Flexibility. International Journal on Theoretical & Applied Research in Mechanical Engineering 2 (1).

Singhose, W., Kim, D., Kenison, M., 2008. Input shaping control of double-pendulum bridge crane oscillations. Journal of Dynamic Systems Measurement and Control-Transactions of the Asme 130 (3).

Singhose, W.E., Porter, L.J., Seering, W.P., 2002. Input shaped control of a planar gantry crane with hoisting. IEEE.

Sun, M., Zhao, T., Wang, S., Han, G., Jin, G., Chen, H., Sun, Y., 2024. Dynamic analysis and experimental research on slender-beam payload swing suppression for marine crane retrofitted a multi-tagline parallel anti-swing system. Ocean Engineering 296, 116922.

Sun, N., Fang, Y., Chen, H., Lu, B., 2017. Amplitude-Saturated Nonlinear Output Feedback Antiswing Control for Underactuated Cranes With Double-Pendulum Cargo Dynamics. IEEE Transactions on industrial electronics.

Sun, N., Wu, Y., Liang, X., Fang, Y., 2019a. Nonlinear Stable Transportation Control for Double-Pendulum Shipboard Cranes With Ship-Motion-Induced Disturbances. Industrial Electronics, IEEE Transactions on.

Sun, N., Yang, T., Chen, H., Fang, Y.C., Qian, Y.Z., 2019b. Adaptive Anti-Swing and Positioning Control for 4-DOF Rotary Cranes Subject to Uncertain/Unknown Parameters With Hardware Experiments. Ieee Transactions on Systems Man Cybernetics-Systems 49 (7), 1309-1321.

Tang, R., Huang, J., 2016. Control of bridge cranes with distributed-mass payloads under windy conditions. Mechanical Systems & Signal Processing 72-73, 409-419.

Vaughan, J., Kim, D., Singhose, W., 2010. Control of Tower Cranes With Double-Pendulum Payload Dynamics. IEEE Transactions on Control Systems Technology 18 (6), 1345-1358.

Wang, J.L., Wang, S.H., Chen, H.Q., Niu, A.Q., Jin, G.L., 2021. Dynamic Modeling and Analysis of the Telescopic Sleeve Antiswing Device for Shipboard Cranes. Mathematical Problems in Engineering 2021.

Wang, Y., Yu, F.J., Li, Q.Z., Chen, Y., 2023. Dual-space configuration synthesis method for rigid-flexible coupled cable-driven parallel mechanisms. Ocean Engineering 271.

Yuan, G.H., Hunt, B.R., Grebogi, C., Ott, E., Kostelich, E.J., 1997. Design and Control of Shipboard Cranes, ASME 1997 Design Engineering Technical Conferences.

Zhai, M., Yang, T., Sun, N., Fang, Y., 2022. Observer-based adaptive fuzzy control of underactuated offshore cranes for cargo stabilization with respect to ship decks. Mechanism and Machine Theory: Dynamics of Machine Systems Gears and Power Trandmissions Robots and Manipulator Systems Computer-Aided Design Methods, 175.

Zhang, X.H., Duan, M.L., Mao, D.F., Yu, Y., Yu, J.X., Wang, Y., 2017. A mathematical model of virtual simulation for deepwater installation of subsea production facilities. Ships and Offshore Structures 12 (2), 182-195.

Zhao, Y., Cheng, Z.S., Gao, Z., Sandvik, P.C., Moan, T., 2019. Numerical study on the feasibility of offshore single blade installation by floating crane vessels. Marine Structures 64, 442-462.